Geological controls on Underground Hydrogen Storage in depleted gas fields

Ana Loyola*[1,3], Denis Voskov[1], Rouhi Farajzadeh[1,2], Kevin Bisdom[2], Karin de Borst[2], and Sebastian Geiger[1]

[1]Faculty of Civil Engineering and Geosciences, Delft University of Technology, Delft, The Netherlands
[2]Shell Global Solutions International B.V., The Hague, The Netherlands
[3]Navier, ENPC, Institut Polytechnique de Paris, Univ Gustave Eiffel, CNRS, Marne-la-Vallée, France

---

Preprint statement

This document is a non-peer reviewed preprint submitted to EarthArXiv. This manuscript has been submitted to *Marine Geoscience and Energy Resources.*

---

*Corresponding author: ana.loyola@univ-eiffel.fr

Geological controls on Underground Hydrogen Storage in depleted gas fields

Ana Loyola[a,c,*], Denis Voskov[a], Rouhi Farajzadeh[a,b], Kevin Bisdom[b], Karin de Borst[b], Sebastian Geiger[a]

[a] *Faculty of Civil Engineering and Geosciences, Delft University of Technology, Delft, The Netherlands*
[b] *Shell Global Solutions International B.V., The Hague, The Netherlands*
[c] *Navier, ENPC, Institut Polytechnique de Paris, Univ Gustave Eiffel, CNRS, Marne-la-Vallée, France*

Abstract

The geological storage of hydrogen is an alternative for large-scale energy storage in support of expanding renewable energy systems. The North Sea has hundreds of depleted gas fields that are potential storage sites. Robust screening procedures are necessary to select the most suitable reservoirs in terms of geology. This study investigates the geological controls on hydrogen storage in depleted natural gas fields of the Bunter sandstone, an important formation in the North Sea. Using an ensemble of geological models and numerical simulations, we assess the impact of structural features and sedimentological heterogeneities on storage performance, as measured by metrics of recovery factor and purity. Key controlling factors include depositional cycle and reservoir thickness, dip, and the lateral continuity of mudstone and aeolian sandstone layers, which mainly influence performance through gravity-driven mechanisms. Building on this insight, a modified gravity number that incorporates heterogeneities is proposed to serve as screening criterion for the selection of top-performing depleted gas fields.

Keywords: Underground Hydrogen Storage, heterogeneity, screening, depleted gas fields, site selection, Bunter sandstone

*Correspondig author
Email address: ana.loyola@univ-eiffel.fr (Ana Loyola)

1. Introduction

Several governments worldwide announced targets to achieve net-zero emissions by 2050. These targets are informing the planning of future energy systems, which are expected to incorporate a higher share of renewable energy sources, including solar and wind. These renewables, however, are weather-dependent and thus intermittent, leading to periods of higher demand than production and vice versa. Hydrogen is a candidate to solve this supply and demand imbalance (Tarkowski, 2019; Zivar et al., 2021). Surplus energy could be used for the low-carbon production of hydrogen and its storage for later use.

The large-scale storage of energy through hydrogen poses an issue of space, especially considering its low volumetric energy density (Navaid et al., 2023). In this context, the underground presents a viable opportunity to achieve large, long-duration storage capacities. Underground Hydrogen Storage (UHS) can be implemented in three main types of geological sites: salt caverns, aquifers, and depleted oil and gas reservoirs.

The use of depleted gas reservoirs, in particular, presents several attractive features. Firstly, they represent 80% of the global gas storage capacity (Tarkowski, 2019). Secondly, their history as gas reservoirs proves that they trapped gas for millions of years and indicates the existence of data and technological expertise on the formation and its operational limits. Thirdly, they have infrastructure already in place that could be reused, and the remaining gas can serve as a cost-free cushion gas.

The North Sea has great potential for seasonal energy storage through UHS for two main reasons. Firstly, countries in the region have expanding renewable energy systems and ambitious projections for future offshore wind energy capacity. The United Kingdom (UK), for example, aims to achieve over 40 GW of offshore wind energy capacity by 2030 (Department of Energy and Climate Change, 2011), and the Netherlands aims at 21 GW by 2032 and 70 GW by 2050 (Cleijne et al., 2020). Secondly, the North Sea hosts several hundred gas fields, many of which will be decommissioned and could be repurposed for UHS.

This large number of gas fields requires systematic screening and ranking procedures to identify the most suitable candidates for UHS. Several studies dedicated to the screening of geological sites for UHS worldwide (e.g. Juez-Larré et al., 2019; Lankof et al., 2024; Safari et al., 2023; Harati et al., 2024; Diamantakis et al., 2024; Okoroafor et al., 2022) converge on a set of basic criteria focused on technical-economical viability, seal integrity and storage capacity. Common criteria include site location, formation thickness and volume, average permeability and porosity, caprock lithology, reservoir dip, temperature, and current reservoir pressure.

In the context of the North Sea region, Juez-Larré et al. (2019) identified 140 depleted gas fields as suitable candidates for UHS in the Netherlands, while Harati et al. (2024) ranked 71 depleted gas fields on the UK Continental Shelf. Thus, the number of suitable gas fields in the region amounts to at least a few hundred, and further levels of screening are necessary to identify the most promising sites.

More in-depth screening and classification can be achieved by accounting for geological heterogeneities, such as sedimentological, structural and petrophysical features, and linking them to performance metrics. Although gas flow is generally less sensitive to heterogeneities than higher-viscosity fluids (Ringrose and Bentley, 2015), studies that incorporate geostatistical models of permeability and examine facies heterogeneity report variability in UHS performance (Pfeiffer et al., 2017; Bo et al., 2024). Despite that, heterogeneities have not yet been systematically integrated into screening criteria for UHS.

Furthermore, most existing screening procedures do not go beyond a qualitative analysis of the sealing potential and a rough estimate of storage capacity, overlooking the effect of geological factors on the performance of cyclic injection and production operations. As an exception, Okoroafor et al. (2022) proposed screening criteria based on the most relevant factors for the productivity index, computed with numerical models of UHS operations in depleted fields. However, these models assume homogeneous reservoirs and, therefore, do not capture the influence of geological heterogeneities on storage performance.

In this study, we investigate the geological controls of UHS in depleted gas fields and quantify their influence on performance. We target the Bunter sandstone as a case study to develop screening tools that are applicable to several potential fields in the North Sea. The Bunter sandstone, or Buntsandstein (as known in the German nomenclature), hosts gas fields in the North Sea sectors belonging to Germany, the Netherlands and the UK; it also holds economic relevance in several other countries of Europe, such as France and Poland, due to its aquifers, oil and gas fields and potential gas storage sites (Newell, 2017). In the Netherlands, for example, the German Triassic Group, of which the Bunter is a subgroup, was responsible for approximately 20% of Dutch gas production (Korevaar et al., 2023).

This work has two main objectives: (1) to identify the main geological controls on the performance of UHS operations in depleted gas fields, considering the key geological heterogeneities of the Bunter sandstone and (2) to propose a general screening and ranking criterion for these fields.

To achieve these objectives, we employ the ensemble of geological models developed by Alshakri et al. (2023) for the Bunter sandstone using a Design of Experiment (DOE) approach. These models present different scenarios for eight key sedimento-

logical heterogeneities of the Bunter, mostly related to the thickness, lateral continuity and permeability of the sedimentological layers. We extend their DOE to incorporate additional geological factors (reservoir thickness, dip and depth) and use the resulting model ensemble to simulate UHS operations. These simulations are used to identify the main geological controls on gas flow behavior and operational performance, as measured by metrics related to storage capacity, recovery, and purity.

This approach, which evaluates geological controls on flow behavior using ensembles of geological scenarios, has previously been applied in studies focused on hydrocarbon recovery (Jackson et al., 2009; Agada et al., 2014; Graham et al., 2015) and carbon capture and storage (Jackson et al., 2022; Alshakri et al., 2023). Here, we apply this methodology for the first time to assess the impact of geological heterogeneities on UHS. We also introduce a modified gravity number that integrates the effects of multiple geological factors and can be used to screen and rank depleted gas fields for performance. While Wang et al. (2022) demonstrated that the gravity number is an effective scaling parameter for hydrogen injection and recovery tests in heterogeneous samples, we generalize it to incorporate a broad range of geological factors and validate its applicability at reservoir-scale operations.

This paper is structured as follows. Section 2 describes the geological models and the Design of Experiment (DOE). Section 3 details the numerical model and presents the computed performance metrics. Section 4 presents the simulation results and discusses the geological controls on the performance of UHS operations. Section 5 introduces the modified gravity number and proposes its use as part of a screening and ranking procedure for depleted gas fields suitable for UHS. Finally, Section 6 summarizes the main conclusions.

2. Geological models

The Buntsandstein formations are aeolian-fluvial sandstones, with fluvial deposits predominantly occurring in the southern North Sea, and highly permeable aeolian deposits becoming predominant northward (van Eijk, 2014; Medici et al., 2018). These formations are characterized by cyclic sequences of sandstones interbedded with claystone and siltstone layers of varying thicknesses (Geluk and Röhling, 1997).

We refer to the synthesis by Alshakri et al. (2023) for a detailed overview of the sedimentology and geological history of the Bunter Sandstone. Based on this review, they developed an ensemble of 32 open-access geological models using a sketch-based approach in the Rapid Reservoir Modeling (RRM) software (Petrovskyy et al., 2023; Jacquemyn et al., 2021). In this study, these models are used to investigate the geological controls on underground hydrogen storage (UHS) operations in depleted Bunter gas fields.

The geological models cover an area of 600 m × 600 m with thickness of 176 m and present different scenarios for the spatial arrangement of six stratigraphic bodies: clay-rich lacustrine mudstone, silty floodplain and sabkha mudstones, sheetflood sandstones, channelized fluvial sandstone, aeolian sandstone, and multistorey, multilateral fluvial sandstone (Figure 1), the latter containing carbonate-cemented basal channel lags. These scenarios are based on eight key sedimentological heterogeneities related to the frequency, thickness, lateral extent and continuity of facies-association layers (Table 1, Figure 1).

Alshakri et al. (2023) designed the models using a resolution IV factorial DOE to evaluate the influence of these eight heterogeneities on reservoir flow behavior. DOE is a statistical method used to quantify the effect of multiple factors on a given response. In a full factorial DOE, all factors are independently varied between low and high values, resulting in 2^n simulations for n factors. To reduce the number of tests, a factorial design can be employed, where only a fraction of the possible combinations are tested. This approach introduces some degree of confounding between effects, depending on the chosen resolution. In the case of the Bunter Sandstone models, the resolution IV reduces the number of tests from 256 to 32, while ensuring that main effects are not confounded with each other, only with three-factor interactions.

We extended the original DOE to include four additional geological factors: permeability of the lacustrine mudstone, reservoir dip, reservoir thickness and reservoir depth. These factors were included because they were shown to be relevant for UHS operations in previous studies (Sainz-Garcia et al., 2017; Bo et al., 2024; Okoroafor et al., 2022). In addition, we combined two of the factors originally analyzed by Alshakri et al. (2023) — the lateral extent and spacing of the carbonate-cemented basal channel lags within the fluvial sandstone — into a single factor. These small-scale heterogeneities are not explicitly represented in the geological models; instead, they are used to compute an equivalent vertical permeability for the fluvial sandstone. Consequently, they were merged into a single variable called the permeability ratio in the fluvial sandbodies.

As a result, the extended analysis includes 11 geological factors evaluated using the same set of 32 geological models. These models capture different combinations of the first 10 factors listed in Table 1 and maintain the resolution IV of the DOE, ensuring that main effects are not confounded with one another. Depth is treated as a special 11th factor: each of the 32 models is simulated at both low and high depth settings. Consequently, the extended DOE consists of 64 simulations in total.

Table 2 presents the DOE, and Table 1 lists the 11 factors along with their low and high settings. The ranges for reservoir thickness, depth, and dip angle were estimated from a comprehensive dataset of well logs and core samples compiled by

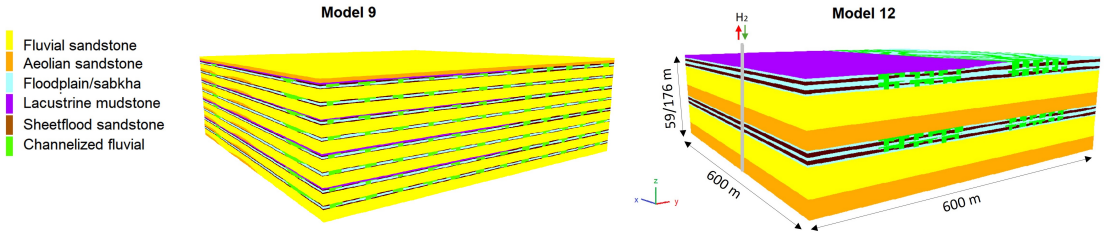

Figure 1: Two examples of geological models built by Alshakri et al. (2023) for the Bunter sandstone. Model 9 has a low thickness of layers and low lateral continuity of all facies association layers. Model 12, on the other hand, has high thickness of layers and high lateral continuity of all facies association layers except the sheetflood sandbodies. The image of Model 12 also depicts the dimensions of the models in the extended DOE and the position of the well used in the simulations of UHS operations.

Korevaar et al. (2023) to generate geological and geophysical property maps of Dutch Triassic reservoirs. Additional details on this estimation process are provided in the Section 1 of the Supplementary Material.

In the models, the reservoir depth influences the initial pressure and temperature of the reservoirs, but is independent of petrophysical properties such as porosity and permeability, as detailed in Section 3.

The high setting for reservoir thickness (176 m) corresponds to the dimensions used in the original geological models by Alshakri et al. (2023). To represent the low thickness setting (59 m) in half of the 32 models, the vertical extent of the original domains is rescaled while preserving the configuration of the stratigraphic bodies (Figure 1). As a result, the thickness of layers (factor A in Table 1) becomes dependent on the total reservoir thickness. Models with the same setting for thickness of layers but different reservoir thicknesses display a similar number of stacking patterns, but the thickness of their individual layers differs.

The approach of systematically varying distinct geological features to assess their influence on reservoir behaviour is well established in the literature (Bentley and Smith, 2008; Jackson et al., 2009; Amy et al., 2013; Graham et al., 2015; Daniilidis et al., 2021; Xinyu et al., 2025). This approach differs from modelling geological heterogeneities in a specific reservoir, typically using geostatistical methods, in that it does not aim to reproduce the geology of a particular site, but instead explores different deterministic and plausible geological scenarios that reflect the range of geological features observed in a target formation. In this study, the DOE-based approach is therefore used to generate multiple deterministic geological scenarios and to evaluate how generic geological features prevalent across the Bunter Formation influence UHS performance.

Table 1: Factors analyzed in the DOE and their high and low setting. Factors A to F were used by Alshakri et al. (2023) to build the ensemble of 32 geological models. We extended the DOE with the remaining geological and petrophysical features. The low and high settings for the thickness of layers have two possible values each. The lowest and highest values correspond to the thickness of the layers for low and high reservoir thickness, respectively. In factor G, k_v and k_h correspond to the vertical and horizontal permeabilities, respectively.

Factor Id	Factor		Low	High
A	Thickness of layers	Fluvial	3.4/10 m	13.3/40 m
		Floodplain/ sabkha	1.7/5 m	6.7/20 m
		Aeolian	1.7/5 m	8.3/25 m
		Lacustrine	0.7/2 m	1.7/5 m
B	Lateral continuity of aeolian bodies		Discontinuous lens	Continuous sheet
C	Lateral continuity of lacustrine layers		Discontinuous sheet	Continuous sheet
D	Proportion of channelized fluvial sandbodies in floodplain/sabkha		17 %	33 %
E	Lateral connectivity of channelized fluvial sandbodies in floodplain/sabkha		Isolated clusters	Connected network
F	Lateral continuity of sheetflood sandbodies in floodplain/sabkha		Discontinuous lens	Continuous sheet
G	k_v/k_h ratio of fluvial sandbodies		0.05	0.5
H	Permeability of lacustrine layers		0.001 mD	0.01 mD
I	Reservoir thickness		59 m	176 m
J	Reservoir dip		0 °	3 °
K	Reservoir depth		1500 m	3000 m

Table 2: DOE composed of 32 different combinations of the factors A to J in Table 1, where L stands for low setting and H for high setting. To assess the impact of depth (factor K), each of these 32 combinations was tested with both the low and the high setting for reservoir depth, resulting in 64 cases.

Models 1-16											**Models 16-32**										
	A	B	C	D	E	F	G	H	I	J		A	B	C	D	E	F	G	H	I	J
1	L	L	L	L	H	L	L	L	L	L	17	L	L	L	L	L	H	L	L	H	H
2	H	L	L	L	H	L	H	H	L	L	18	H	L	L	L	L	H	H	H	H	H
3	L	H	L	L	L	L	H	H	L	L	19	L	H	L	L	H	H	H	H	H	H
4	H	H	L	L	L	L	L	L	L	L	20	H	H	L	L	H	H	L	L	H	H
5	L	L	H	L	L	L	L	H	L	H	21	L	L	H	L	H	H	L	H	H	L
6	H	L	H	L	L	L	H	L	L	H	22	H	L	H	L	H	H	H	L	H	L
7	L	H	H	L	H	L	H	L	L	H	23	L	H	H	L	L	H	H	L	H	L
8	H	H	H	L	H	L	L	H	L	H	24	H	H	H	L	L	H	L	H	H	L
9	L	L	L	H	L	L	H	L	H	L	25	L	L	L	H	H	H	H	L	L	H
10	H	L	L	H	L	L	L	H	H	L	26	H	L	L	H	H	H	L	H	L	H
11	L	H	L	H	H	L	L	H	H	L	27	L	H	L	H	L	H	L	H	L	H
12	H	H	L	H	H	L	H	L	H	L	28	H	H	L	H	L	H	H	L	L	H
13	L	L	H	H	H	L	H	H	H	H	29	L	L	H	H	L	H	H	H	L	L
14	H	L	H	H	H	L	L	L	H	H	30	H	L	H	H	L	H	L	L	L	L
15	L	H	H	H	L	L	L	L	H	H	31	L	H	H	H	H	H	L	L	L	L
16	H	H	H	H	L	L	H	H	H	H	32	H	H	H	H	H	H	H	H	L	L

3. Numerical model

The open-source Delft Advanced Research Terra Simulator (open-DARTS) (Voskov et al., 2024) is used to simulate UHS operations in the ensemble of geological models. The open-DARTS framework has been benchmarked for several complex flow and transport phenomena, including non-isothermal, multiphase, multicomponent, and reactive flow, with a focus on various geoenergy applications (Wang et al., 2020; Flemisch et al., 2024; de Hoop et al., 2024; Nordbotten et al., 2025).

The numerical model is used to compute performance metrics for UHS and to assess the influence of geological features (factors) on these outcomes. Below, Section 3.1 presents the formulation of the problem, Sections 3.2 to 3.5 present the setup

of the numerical model and Section 3.6 presents the computed performance metrics.

3.1. Mathematical models

The reservoirs are considered to be depleted gas reservoirs initially saturated with methane ($\mathsf{CH_4}$) and not connected to any aquifer. The flow problem is described by the mass conservation of one-phase (gas) and two components, hydrogen ($\mathsf{H_2}$) and methane ($\mathsf{CH_4}$), as given by

$$\frac{\partial(\phi\, x_c\, \rho_g)}{\partial t} + \nabla \cdot (x_c\, \rho_g\, \boldsymbol{u}_g + \phi\, \rho_g\, \boldsymbol{J}_c) - q_c = 0. \tag{1}$$

Here, the subscript c denotes a component, the subscript g refers to the gas phase, ϕ is effective rock porosity, x_c is the molar concentration of component c, ρ_g is the molar density of the gas phase, $\boldsymbol{u}_g$ is the velocity of the gas phase, $\boldsymbol{J}_c$ is diffusive flux of component c and q_c denotes source of the component c.

The phase velocity $\boldsymbol{u}_g$ is given by Darcy's law as

$$\boldsymbol{u}_g = -\frac{\boldsymbol{K}}{\mu_g}(\nabla p_g - \rho_g \boldsymbol{g}), \tag{2}$$

where $\boldsymbol{K}$ is the intrinsic permeability tensor, μ_g is gas phase viscosity and $\boldsymbol{g}$ is the gravity vector. The diffusive flux $\boldsymbol{J}_c$ is given by Fick's law as

$$\boldsymbol{J}_c = -D_c \nabla x_c, \tag{3}$$

where D_c is the molecular diffusion coefficient of component c.

The numerical model employs a Fully Implicit method and cell-centered Finite Volume Two Point Flux approximation scheme to discretize (1) in time and space, respectively. All simulations were performed using the open-DARTS framework on the DelftBlue supercomputer (Delft High Performance Computing Centre , DHPC).

3.2. Initial Conditions

Assuming hydrostatic pressure and an average water density of 1000 kg/m^3, the original reservoir pressures are estimated to be 150 bar for the low depth setting (1500 m) and 300 bar for the high depth setting (3000 m). To represent depleted conditions prior to UHS operations, we applied a depletion factor of two-thirds of the original pressure. This results in initial pressures of 50 bar and 100 bar for the low and high depth scenarios, respectively.

Reservoir depth also affects the temperature settings in the model. Using a linear regression of the borehole temperature data from the Netherlands Oil and Gas

Portal (NLOG), the reservoir temperatures were estimated as 55 °C for the low depth cases and 104 °C for the high depth ones (Figure S2). Although the model assumes isothermal conditions, temperature influences fluid properties and therefore plays a role in the simulations.

3.3. Fluid and rock properties

The density of the gas mixture of CH_4 and H_2 is calculated using the Peng-Robinson equation of state. The viscosity of the gaseous mixture is estimated from the dataset provided by Hassanpouryouzband et al. (2020), which was computed using the SuperTRAPP model (Huber, 2018). For the viscosity of pure H_2 and pure CH_4, we use the dataset provided by the NIST Chemistry WebBook (Lemmon et al., 2025). These datasets provide viscosity values for a range of states defined by pressure, temperature, and fluid composition. A multi-linear interpolation scheme is used in open-DARTS to estimate flux operators (see Lyu et al., 2021, for details), including gas viscosity for arbitrary states based on this data. Figure S3 presents fluid density and viscosity for the pressure and temperature ranges relevant to the numerical model.

Table 3 lists the porosity and permeability values assigned to the different geobodies. These values are mostly similar to those used by Alshakri et al. (2023) and align with porosity–permeability relationships derived from core measurements of Triassic formations in the Netherlands (van Kempen et al., 2018). The horizontal permeability of the fluvial sandbodies is fixed across all models, while the vertical permeability is adjusted according to the permeability ratio in the fluvial sandbodies defined in the DOE. For the lacustrine mudstone, a range of permeability values representative of clay-rich materials was adopted to evaluate how the mudstones could act as flow barriers in the reservoir.

For the diffusive flux (Equation 3), a constant molecular diffusion coefficient was computed using the correlation proposed by Kobeissi et al. (2024) for H_2-CH_4-sandstone systems. This correlation is a function of pressure and temperature, which in turn depend on reservoir depth. The input temperature is the constant temperature estimated for each depth setting and the input pressure is the average of the minimum and maximum bottom-hole pressures (Table 4 in Section 3.5). This approach yielded diffusion coefficients of 0.078 m^2/day for the low-depth models and 0.057 m^2/day for the high-depth models.

3.4. Domain and mesh

A fully structured grid was used in all simulations. To ensure a consistent level of numerical diffusion, identical grid cell dimensions were used across all models.

Table 3: Intrinsic permeability and porosity of the sedimentological bodies present in the Bunter sandstone models.

Geobody	Porosity (%)	Permeability (mD)
Lacustrine mudstone*	5	0.001-0.01
Floodplain and sabkha mudstone	7	1
Sheetflood fluvial sandstone	15	200
Fluvial sandstone**	17	500
Aeolian sandstone	24	3000

* Lacustrine permeability is a factor in the DOE

** Permeability in horizontal directions

These dimensions were determined through mesh sensitivity studies using the flow diagnostics module in RRM (Petrovskyy et al., 2023).

The final cell dimensions were 8.45 m x 8.45 m x 0.45 m. As a result, the mesh contains $71 \times 71 \times 132$ cells in the low-thickness models and $71 \times 71 \times 396$ cells in the high-thickness models.

The selected mesh resolution allows an accurate representation of the dip angle in the models with a high setting of reservoir dip. The dip angle is defined as the angle between the x-direction and the longitudinal axis of the reservoir. To impose this inclination, the original geological models were modified in open-DARTS by incrementally elevating columns of grid cells in a step-wise manner (Figure 2).

3.5. Boundary conditions and well constraints

The reservoir boundaries are closed (no-flow) in all simulations. The UHS operations are carried out using a single vertical well, which is fully perforated over the entire thickness of the reservoir. The well is positioned close to the minimum x-coordinate and centered along the y-axis (Figure 1), ensuring an updip location when dip is present. The UHS operation consists of two phases. Initially, there is a period of injection of hydrogen as cushion gas. This initialization period lasts approximately six months, and is terminated when a minimum bottom-hole pressure (BHP) is reached. Subsequently, six annual cycles are simulated, each comprising a six-month injection period followed by three-month idle and withdrawal phases.

The injection and withdrawal target rates were defined to achieve full storage and recovery capacities within the operational constraints of BHP. The operational flow rates and BHPs are presented in Table 4 for reservoirs with a 59 m thickness

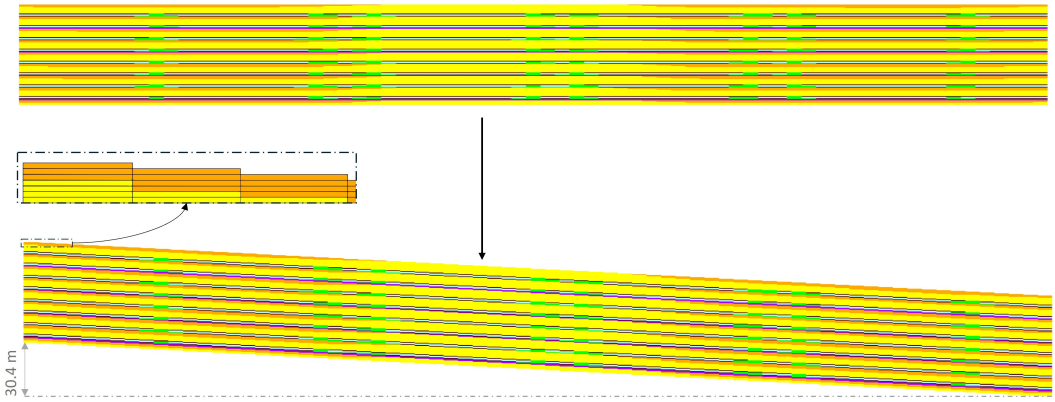

Figure 2: Procedure to add dips in the reservoir models. The grid cells are elevated in a step-wise manner along the x-direction, resulting in a maximum elevation of 30.4 m of the bottom of the reservoir.

(corresponding to the low setting for reservoir thickness). For the models with the high reservoir thickness, the target rates were multiplied by three, in accordance with the threefold increase in thickness. This approach ensures that a similar number of pore volumes of hydrogen is injected at comparable injection velocities across all models with the same depth. The recovery rates in the cycles are twice the target injection rate because the withdrawal phase lasts half as long as the injection phase. In standard units, the target injection rate corresponds to 1.2 million sm^3/day for the low depth case and 1.9 million sm^3/day for the high depth case.

The pressure constraints are depth-dependent. The maximum allowable BHP is set to the estimated original (pre-depletion) reservoir pressure of 150 bar for the low depth setting (1500 m) and 300 bar for the high depth setting (3000 m). The minimum BHP was fixed at half of the maximum value, resulting in operational pressure ranges of 75 to 150 bars for low depth cases and 150 to 300 bars for high dip cases.

To compute well pressures and flow rates, the Peaceman well model is used, assuming a well diameter of 16 cm. The target flow rate is imposed on the well and maintained during each injection or withdrawal phase unless the BHP reaches its operational limit, in which case the flow rate is adjusted accordingly.

3.6. Performance metrics

Four performance metrics are computed in all simulations: cycle recovery factor (RF), ultimate recovery factor (ultimate RF), cycle mass purity (MP) and flow purity

Table 4: Operational constraints used in the simulations of the low and high-depth models, including target injection rate in the one-year initialization period (q_{init}), target injection (q_{inj}) and recovery (q_{rec}) rates during cyclic operation, and minimum and maximum BHPs. The target rates refer to the models with low reservoir thickness; for the high-thickness cases, the values are scaled accordingly.

	Low depth	High depth
q_{init} (Mmol/day)	35	56
q_{inj} (Mmol/day)	52	84
q_{rec} (Mmol/day)	104	168
Max/min BHP (bar)	75/150	150/300

(FP). The Recovery Factor (RF) of cycle i is given by:

$$RF^i = \frac{M^i_{recH2}}{M^i_{injH2}}, \tag{4}$$

where M^i_{recH2} and M^i_{injH2} are the recovered and injected mass of hydrogen, respectively, in cycle i, respectively. The ultimate RF is computed as:

$$RF = \frac{\sum_i M^i_{recH2}}{\sum_i M^i_{injH2}}, \tag{5}$$

Note that the ultimate RF accounts only for the total injection and recovery of hydrogen in the cyclic operations, and does not consider the initialization period.

The mass purity (MP) of cycle i is given by:

$$MP^i = \frac{M^i_{recH2}}{M^i_{rec}}, \tag{6}$$

where M^i_{recH2} and M^i_{rec} are the recovered mass of hydrogen and total recovered mass of fluids in cycle i, respectively. The flow purity FP at time t of the withdrawal phase of cycle i is given by:

$$FP^i(t) = \frac{Q^i_{recH2}(t)}{Q^i_{rec}(t)}, \tag{7}$$

where Q^i_{recH2} and Q^i_{rec} are outflow rates of hydrogen and total outflow rates in the withdrawal phase of cycle i, respectively.

4. Geological controls on the performance of UHS

This section presents the results of the UHS simulations conducted for the ensemble of geological models, with a focus on evaluating the influence of geological factors on performance and flow behavior.

Section 4.1 presents an analysis of the 32 simulations carried out using the low-depth setting. Section 4.2 presents results for the high-depth models and discusses the impact of depth on UHS operations. Depth is treated as a separate case study because, unlike the other geological factors, it does not alter the geological domain or petrophysical properties, but affects the thermodynamic state and operational conditions instead. Finally, Section 4.3 presents a comparison between our findings and the conclusions of previous works.

4.1. Low-depth models

Section 4.1.1 presents the performance metrics obtained for the low-depth models. Section 4.1.2 presents an analysis of general performance trends and flow mechanisms of the model ensemble, and Section 4.1.3 provides an interpretation of the influence of geological factors on flow behavior and operational performance.

4.1.1. Performance metrics results

Figure 3 shows the evolution of flow purity (FP) during the withdrawal periods, and Figure 4 presents the recovery factor (RF) and mass purity (MP) per cycle for the ensemble of low-depth models. The Supplementary Material presents additional results that support interpretation, including the production of methane (Figure S4) and the evolution of the average reservoir pressure (Figure S5) for the model ensemble.

The range of variation of the performance metrics (RF, MP and FP) decreases with increasing operation cycles. The minimum flow purity ranges from 61% to 80% in Cycle 1, but narrows to 85% to 95% by Cycle 6 (Figure 3). The cycle recovery factor varies between 70% and 96% in Cycle 1 and between 96% and 98% in Cycle 6. The mass purity follows a similar trend, varying between 71% and 96% in Cycle 1 and between 96% and 98% in Cycle 6 (Figure 4). Clearly, the minimum values of the performance metrics increase as the number of cycles increases. From Cycle 1 to Cycle 6, the minimum values of FP, RF and MP increase by 24%, 26% and 25%, respectively.

The RF and MP remain below 100 % because some of the initially-in-place methane (CH_4) is produced. For the model ensemble, the production of CH_4 decreases with increasing cycles (Figure S4). In the first withdrawal, the production

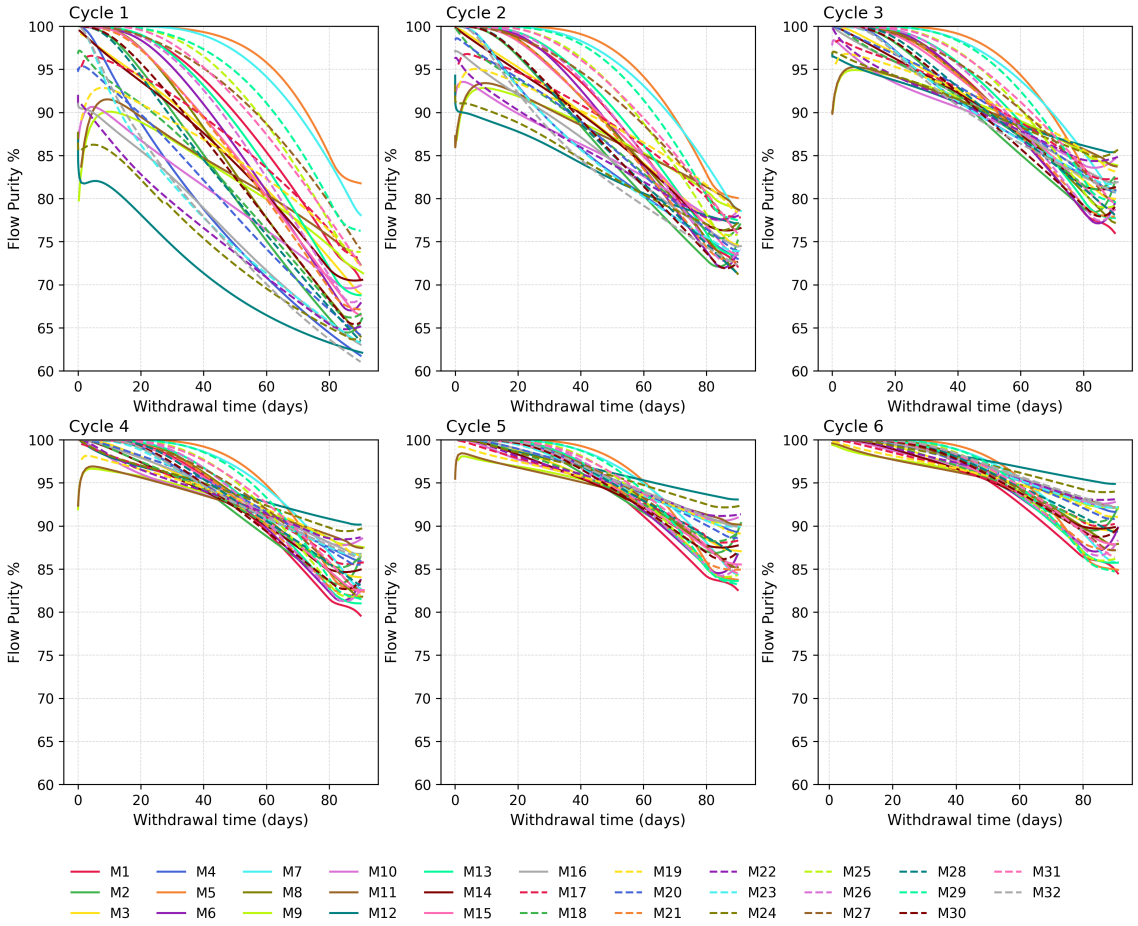

Figure 3: Evolution of the flow purity during the withdrawal periods for the ensemble of Bunter sandstone models. The upward shift by the end of withdrawal in some models corresponds to the moments where borehole pressure constraints are reached and well rates are decreased.

of CH_4 normalized by reservoir thickness varies between 5 and 48 millions mol/m, while in the last cycle, it varies between 3 and 6 millions mol/m.

Table 5 presents the minimum, maximum, and average values for total H_2 injection, normalized by reservoir thickness, and for the ultimate RF. On average, 0.90 Gmol of H_2 per meter of thickness was stored during the cyclic operations. Considering the High Heating Value (HHV) of H_2 (39.4 kWh/kg) and the maximum reservoir thickness of 176 m, this corresponds to an average of 12.6 TWh of maximum stored energy in six years of operation.

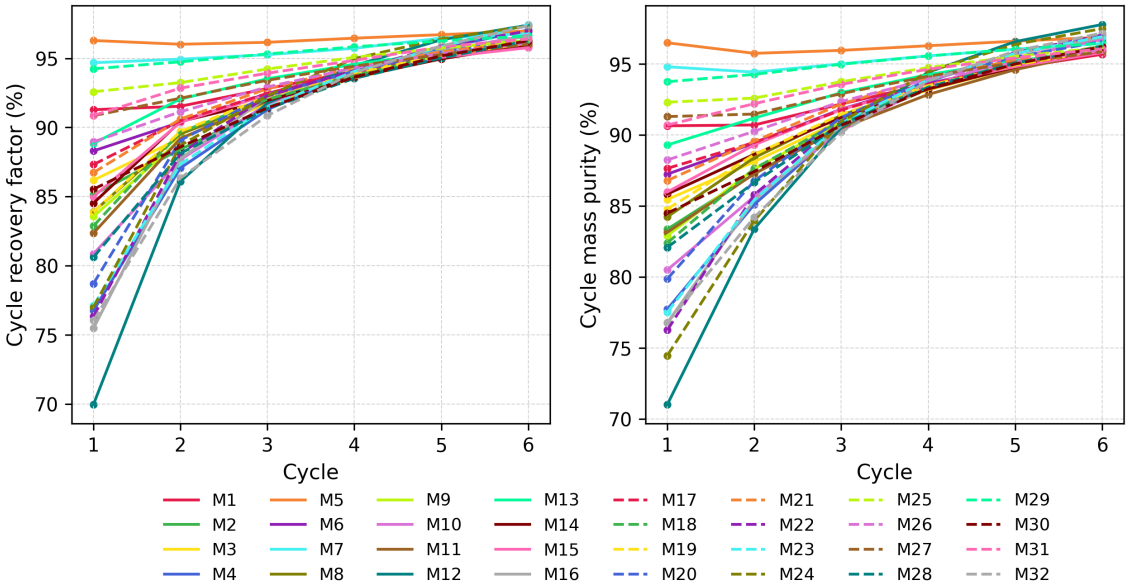

Figure 4: Evolution of the cycle recovery factor (left) and mass purity (right) during the withdrawal periods for the ensemble of Bunter models.

Table 5: Minimum, maximum and average total injection of hydrogen, normalized by reservoir thickness, and ultimate recovery factor for the low-depth models. These quantities do not consider the hydrogen injected as cushion gas in the initialization period.

	Min.	Max.	Average
Norm. total injection (Gmol/m)	0.86	0.95	0.90
Ultimate Recovery Factor (%)	89.7	96.7	92.5

4.1.2. General flow behavior

It is possible to recognize a set of flow mechanisms that govern the general performance trends of the model ensemble. They are the following:

- Gas compression and expansion: The average reservoir pressure of the model ensemble closely follows the imposed BHP limits, with small pressure gradients in the reservoir (Figures S5 and S6). This indicates that hydrogen injection and production are primarily controlled by the compression and expansion of the gas in place, with the gas density varying between its maximum and minimum values within the BHP constraints (as exemplified for Model 1 in FigureS6).

- Flow compartmentalization: The repeating pattern formed by interbedded sandstones and mudstone layers compartmentalizes the reservoir. The low-permeability mudstones hinders vertical communication, separating the hydrogen plumes into distinct compartments. Throughout this paper, we refer to each of these repeating sandstone-mudstone couplets as depositional cycles or compartments. As an example, Figure 7 depicts the two depositional cycles in Model 12 and show how the H_2 plume is segmented by these compartments. Note that models with low setting for the thickness of layers, such as Model 9 (Figure 1) have 8 to 9 depositional cycles.

- Gravity effects: Upon injection, H_2 flows in an unstable displacement front due to its significantly lower density and viscosity compared to CH_4 (Figure S3, Table 8). This leads to gravity override. A cross-section of Model 12 (Figure 7) shows a typical example, with the H_2 plume spreading more laterally near the top of each compartment than at the bottom.

- Replacement of methane and mixing: The instability of the H_2 front leads to the production of CH_4. This production decreases with increasing cycles (Figure S4), because as more CH_4 is produced, H_2 becomes the dominant component in the reservoir. The replacement of CH_4 by H_2 reduces the extent of impurity and weakens gravity-driven effects. These effects explain the general improvement in performance with increasing cycles (Figures 3 and 4).

4.1.3. Impact of geology on flow and performance

The variability observed in the performance metrics (Figures 3 and 4) is due to the different combinations of geological factors in each model. The fact that the range of variation of these metrics decreases with increasing cycles indicates that the geological heterogeneities become less impactful on the performance as the UHS operation continues.

This is illustrated in Figure 5 for Model 12. After the first injection, H_2 predominantly invades high-permeability zones, with its distribution strongly affected by stratigraphic heterogeneities. By Cycle 6, however, the hydrogen plume becomes nearly insensitive to geological heterogeneities (Figures 7 and 5). At this stage, sufficient time has passed for H_2 to penetrate the low-permeability layers, driven by advection and diffusion.

Figure 6 presents tornado plots for the RF and MP in Cycle 1, and for the total injected and recovered mols of H_2, normalized by reservoir thickness. The performance metrics of Cycle 1 were selected for the sensitivity analysis because

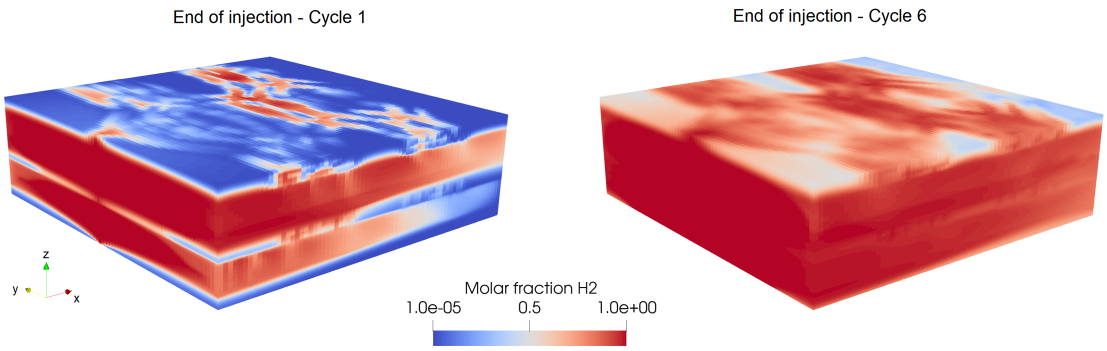

Figure 5: Three-dimensional view of the molar composition of H_2 in Model 12 after the first and last injections. See Figure 1 for the reservoir architecture of Model 12.

early stages of the operation are the most critical for evaluating performance, since they present higher variability of performance (Figures 3 and 4).

Three factors are the most impactful on the RF and MP of Cycle 1: reservoir thickness, thickness of layers, and reservoir dip. They are followed by three stratigraphic heterogeneities: continuity of aeolian bodies, the permeability ratio of the fluvial sandstones, and the continuity of lacustrine mudstones, respectively. The continuity of aeolian bodies also stands out as the most influential factor on the total injected and recovered amounts. The following sections discuss the impact of these geological factors on flow behavior and performance.

4.1.3.1 Thickness and reservoir dip

The importance of reservoir thickness, the thickness of the layers and the reservoir dip is related to gravity effects. Lower reservoir and layer thickness result in thinner reservoir compartments, which reduce buoyancy forces and mitigate gravity override. This comes with the underlying assumption that the thin compartments are connected to the well.

As for reservoir dip, it helps segregate H_2 at the top of the reservoir, while CH_4 remains in the deeper parts of the reservoir. In the high-dip models, methane must migrate updip and overcome gravitational forces to reach the well, being produced more slowly than it would if there was no dip.

These effects are visualized when comparing the H_2 plumes in Models 5 and 12, which are depicted in Figures 8 and 7, respectively. Model 5 has low reservoir thickness, low thickness of the layers and high dip. On the other hand, Model 12 has high reservoir thickness, high thickness of the layers and low dip. The favorable

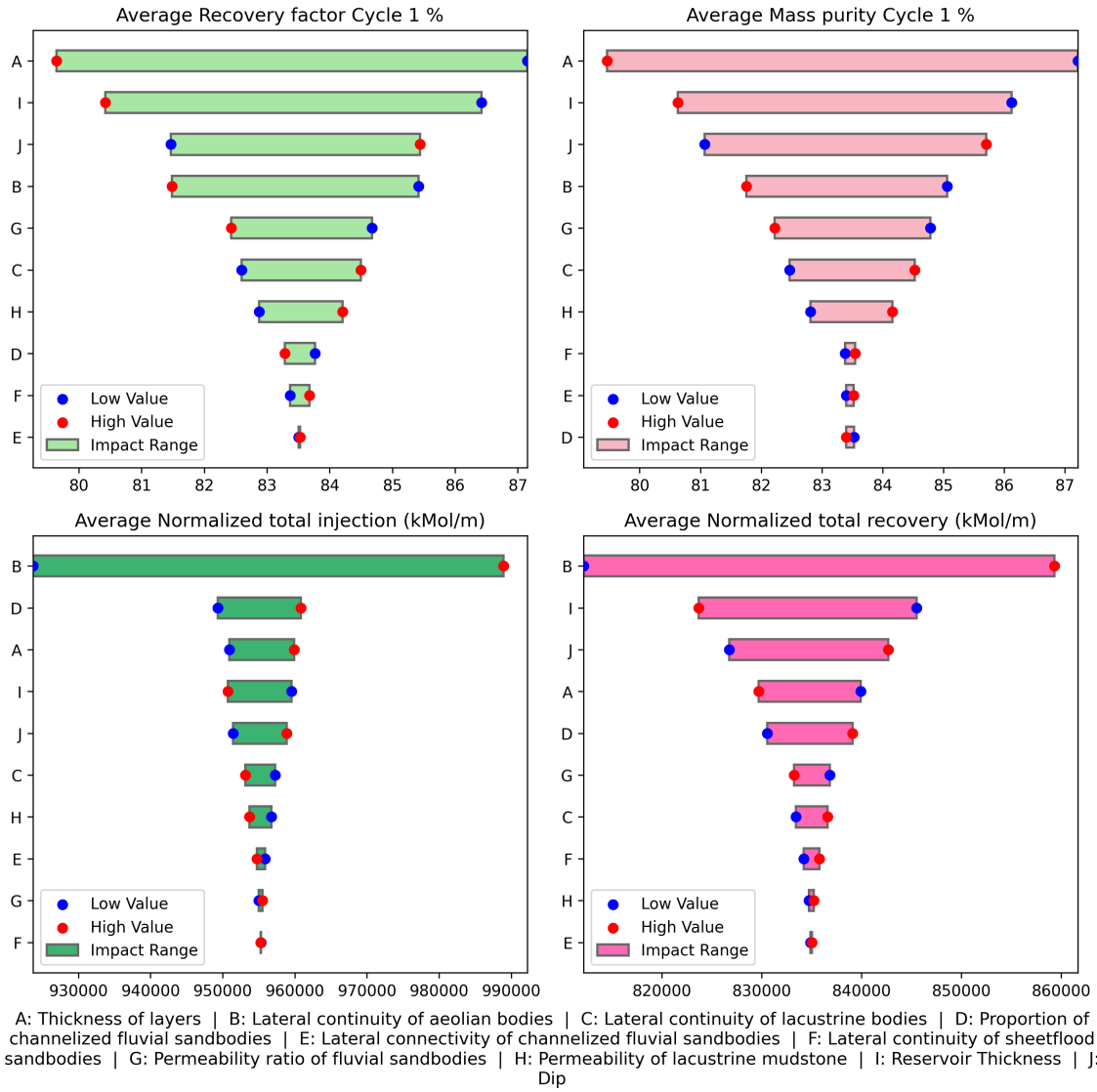

Figure 6: Tornado charts showing the range of variation of the average recovery factor (a) and mass purity (b) of Cycle 1 and the total injection (c) and total recovery (d) of hydrogen normalized by reservoir thickness when the factors are varied between their low and high setting.

geological scenario of Model 5 leads to an additional RF of 26% in Cycle 1, with respect to Model 12 (Figure 4). Also, Models 5 and 12 correspond to the maximum and minimum ultimate RF in Table 5, respectively.

Model 12 produces eight times more CH_4 in Cycle 1 than Model 5 (Table 6),

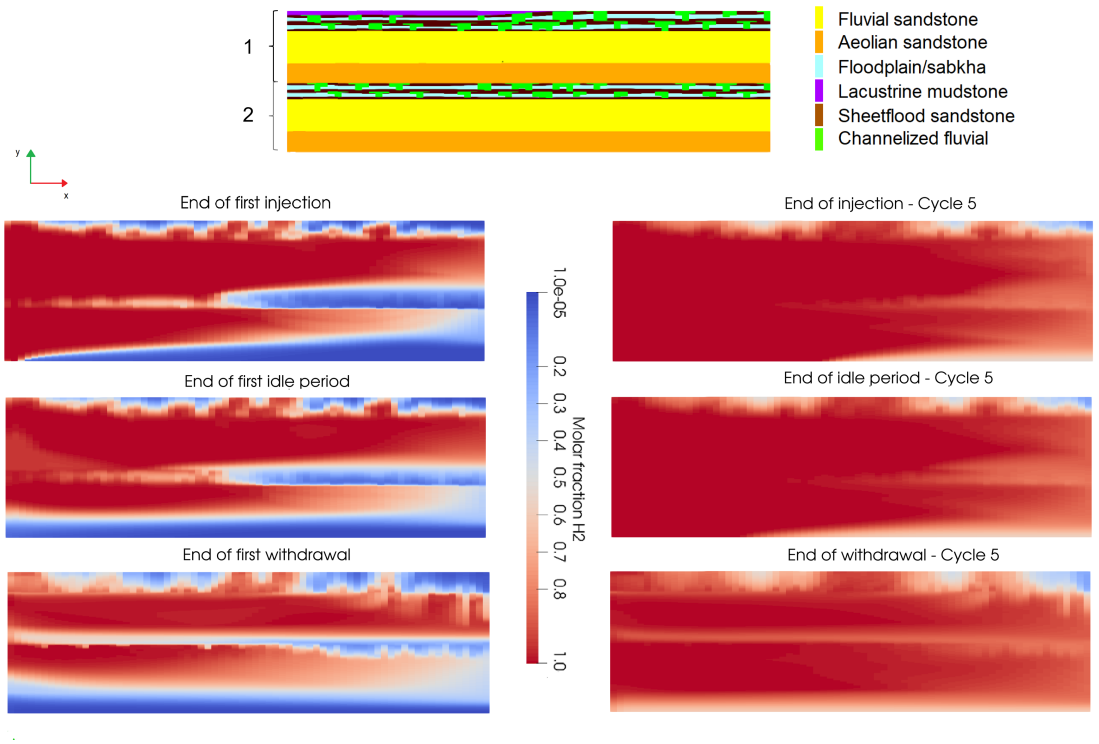

Figure 7: Cross-sectional view of the geobodies (top) and the molar composition of H_2 in Model 12 after the first (lower left) and last (lower right) injection, idle, and withdrawal periods, respectively. The top image shows the two depositional cycles, formed by interbedded sandstone and mudstone layers.

which leads to its lower performance. The high recovery of methane is driven by the remarkably unstable fronts created by gravity override (Figure 7), which is boosted by higher thickness of the layers and low dip. On the other hand, the early high production of CH_4 leads to a fast replacement of CH_4 by H_2, making Model 12 the top-performing one in terms of MP and RF in Cycle 6. The effects of this purification are more clear in Figures 7 and 5, which show that, by Cycle 6, H_2 is the dominant fluid in Model 12.

The gravity override is significantly reduced in Model 5 because of its thin depositional cycles. The more stable fronts between H_2 and CH_4 (Figure 8), combined with the benefit of dip, lead to consistently low production of CH_4 during the operation (Table 6). As a result, Model 5 undergoes smaller changes in plume distribution between the first and last injections, and presents stable performance metrics over

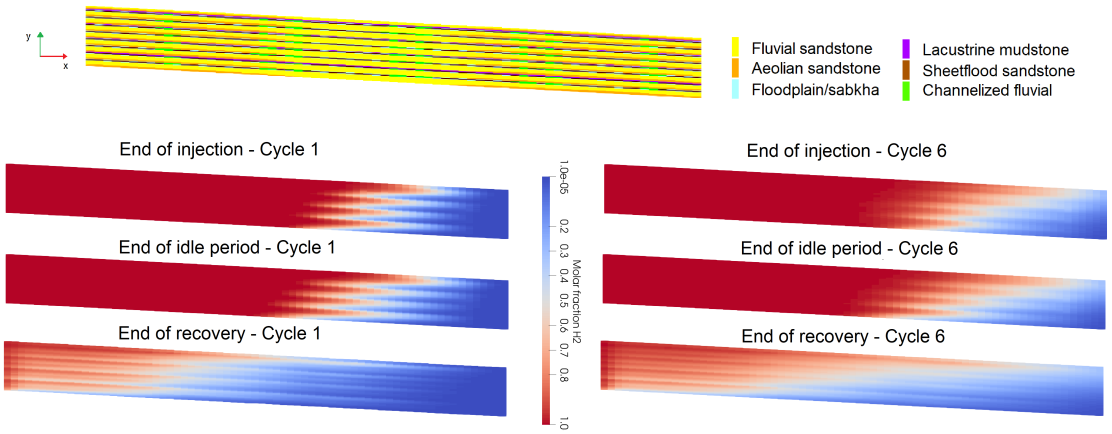

Figure 8: Cross-sectional view of the geobodies (top) and of the molar composition of H_2 in Model 5 after the first (lower left) and last (lower right) injection, idle and withdrawal periods, respectively.

time (Figure 4), with RF and MP always above 95 %.

Table 6: Methane production normalized by reservoir thickness for Models 5 and 12 in cycles 1 and 6.

	Norm. Production of CH_4 (Mmol/m)	
	Cycle 1	Cycle 6
Model 5	5.8	4.6
Model 12	47.9	3.4

4.1.3.2 Continuity of the lacustrine mudstones

Three models - Models 5, 7, and 29 - maintain a recovery factor and mass purity above 93% in all simulated cycles (Figure 4). In terms of flow purity (Figure 3), these models display concave-downward curves, on which the purity remains close to 100% for a period before undergoing a rapid drop, triggered by the onset of methane production.

These three top-performing models have three common geological factors: low total reservoir thickness, low thickness of the facies-association layers, and high lateral continuity of the lacustrine bodies. The continuous lacustrine layers enhance and prolong vertical compartmentalization, helping to mitigate the gravity override.

This enhanced compartmentalization is evident in Figure 9, which compares the H_2 plume for models 1 and 31. These models present similar settings for thickness but different settings for the continuity of the lacustrine bodies. The continuous lacustrine layers in Model 31 create a strong vertical compartmentalization that mitigates gravity override, compared to Model 1, in which the lacustrine layers are discontinuous (Figure 9).

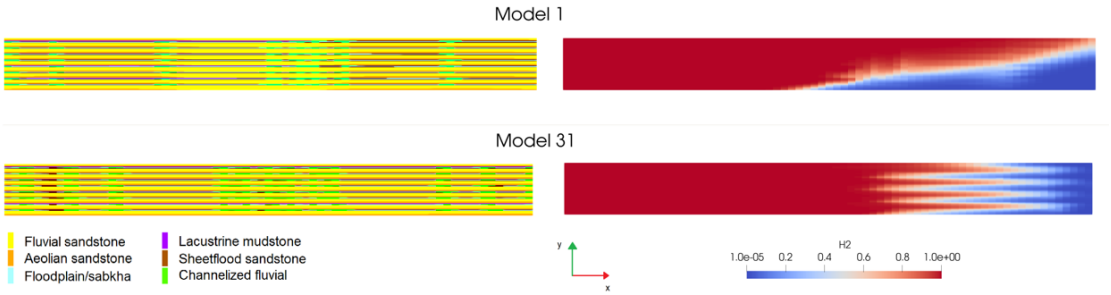

Figure 9: Cross section view of the geobodies (left) and of the molar composition of H_2 (right) in Models 1 and 31 after the first injection. The lacustrine mudstone has low lateral continuity in Model 1 and high lateral continuity in Model 31. As a result, the flow is more compartmentalized in Model 31.

4.1.3.3 Continuity of aeolian bodies and permeability ratio of fluvial bodies

After the thickness of the layers, the most influential sedimentological heterogeneity for RF and MP is the continuity of the aeolian bodies. A high lateral continuity of the aeolian bodies is unfavorable to both RF and MP in Cycle 1 (Figure 6). As shown in Figure 10, the high and low settings for this factor produce two distinct clusters in terms of equivalent longitudinal permeability and average reservoir porosity. Models with high aeolian continuity exhibit an average upscaled permeability of 1043 mD and an average porosity of 16.5 %, while models with low continuity show values of 533 mD and 15.3%, respectively. These upscaled values of permeability were computed in RRM using flow-based upscaling.

The increased longitudinal permeability in models with high continuity of the aeolian bodies promotes the lateral spreading of hydrogen and enhances methane migration toward the well. This behavior is exemplified in Figure 11, where the methane front in Model 32 — which has high continuity of aeolian bodies — is slightly more advanced toward the well compared to Model 30, which has a discontinuous lens of the aeolian sandstone.

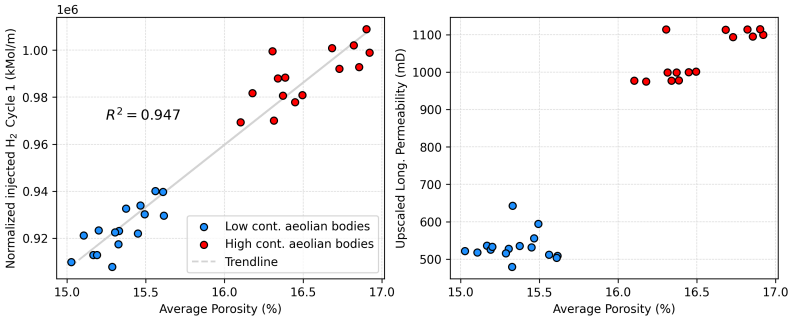

Figure 10: Clustering of average porosity and horizontal permeability (left) and total injected amount of H_2, normalized by reservoir thickness (right). Note that the continuity of the aeolian bodies is the key stratigraphic feature controlling these distributions.

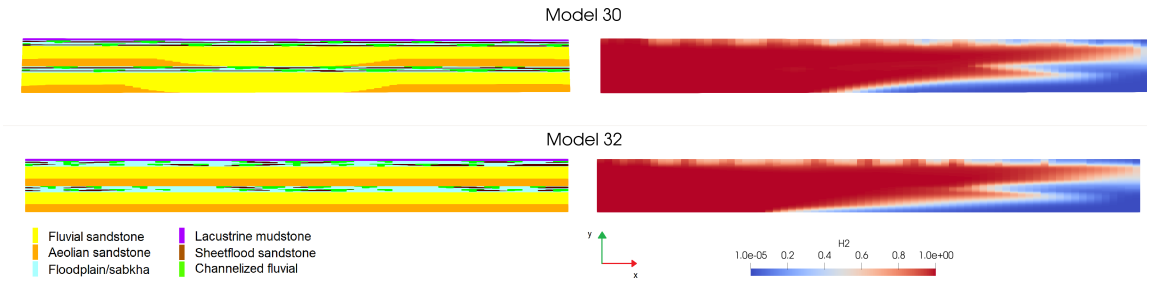

Figure 11: Cross-sectional view of the geobodies (left) and of the molar composition of H_2 (right) in Models 30 and 32 after the first injection. The aeolian sandstone has low lateral continuity in Model 30 and high lateral continuity in Model 32. As a consequence, the methane front advances more towards the well in Model 32.

Nevertheless, the higher porosity associated with the continuous aeolian bodies leads to a higher storage capacity. For that reason, this is the most impactful factor on the total injected mass of hydrogen (Figure 6), which correlates strongly with the average porosity (Figure 6). It is also the most influential factor on the total amount of the recovered hydrogen (Figure 6), as the recovery benefits from the higher equivalent permeabilities and greater amounts of stored hydrogen.

The average storage capacity is 7% higher in models with high continuity of the aeolian bodies than in models with low continuity of the aeolian bodies. This is due to the 1.2% higher average porosity in models with continuous aeolian bodies. In contrast, the recovery factor in the first cycle is on average 4 % lower than in the scenarios with low continuity of the aeolian bodies (Figure 6).

Another geological factor that affects performance because of petrophysical properties is the permeability ratio of the fluvial sandstones. Lower vertical permeabilities

retard the travel of H_2 to the top of the reservoir, mitigating gravity effects and improving performance (Figure 6). The vertical permeability of the fluvial sandbodies increases ten times between its low and high setting (Table 1), while the high continuity of the aeolian bodies increases the longitudinal permeability by a factor of two (Figure 10). Still, the continuity of the aeolian bodies is more influential on the performance (Figure 6), suggesting that the longitudinal component of the permeability is more relevant than the vertical one.

4.2. Impact of reservoir depth

In UHS operations, achieving higher depths can be a resource to increase storage capacity. Comparing two reservoirs with similar pore volumes and different depths, the deeper reservoir can sustain higher working pressures, resulting in a higher working density of H_2.

Table 7 presents the average injected amount of hydrogen, normalized by the reservoir thickness, and the average ultimate recovery factor, for the high-depth models. The average normalized injection increases by a factor of 1.6, from 0.9 to 1.45 Mmol/m, when doubling the depth from 1500 m to 3000 m (Table 5 and Table 7). Considering the HHV for H_2, this means, for a 176-m-thick reservoir, a maximum additional stored energy of 7.3 TWh in 6 years of operation.

Table 7: Minimum, maximum and average total injection of hydrogen, normalized by reservoir thickness, and ultimate recovery factor for the high-depth models. These quantities do not consider the hydrogen injected as cushion gas in the initialization period.

	Min.	Max.	Average
Norm. total injection (Gmol/m)	1.38	1.54	1.45
Ultimate Recovery Factor (%)	89.4	96.2	91.8

Figure 12 presents the average, minimum, and maximum RF and MP per cycle for the low- and high-depth settings. These metrics are lower when the depth is higher, with a maximum difference of 1.7 % in the cycle RF.

The lower performance associated with the high depth can be partially explained by the initial proportion of methane and hydrogen at the beginning of the cyclic operation. By the end of the first one-year injection period, the reservoirs at high depth have, on average, 65% of their pore volume occupied by hydrogen, compared to 69% for the low depth cases.

This difference in the initial H_2 distribution is due to the higher compressibility of CH_4 in the low-depth setting. Table 8 shows the density of methane at the initial

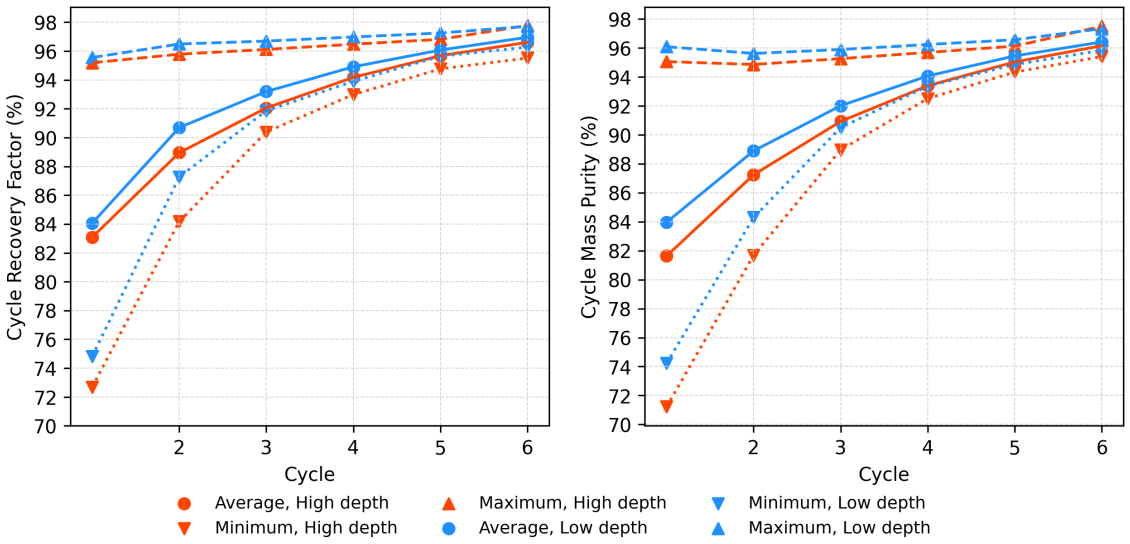

Figure 12: Average, minimum and maximum values for the recovery factor and mass purity per cycle for the low and high depth scenarios.

pressure, and at the minimum and maximum BHPs for both depth settings. Between the initial pressure and the maximum BHP, the density of CH_4 increases by a factor of 3.2 at the low depth setting and 2.9 at the high depth setting, despite the pressure range in the latter being higher. Consequently, when the maximum BHP is reached, a higher proportion of the reservoir pore volume is available for the storage of hydrogen at the low depth.

Table 8: Density of methane (ρ_{CH4}(kg/m^3)) and hydrogen ρ_{H2}(kg/m^3), and their density difference ($\Delta\rho$(kg/m^3)) at the initial, minimum bore hole and maximum bore hole pressures, respectively, in the high and low depth scenarios. These data were retrieved from the NIST Chemistry WebBook (Lemmon et al., 2025).

	Low depth (T = 55 °C)			High depth (T = 104 °C)		
Pressure (bar)	50	75	150	100	150	300
ρ_{CH4}(kg/m^3)	31.6	48.8	102.2	54.6	82.6	157.1
ρ_{H2}(kg/m^3)	3.6	5.4	10.5	6.2	9.2	17.3
$\Delta\rho$(kg/m^3)	28.0	43.4	91.7	48.4	73.4	139.8

Another potential source of differences is the higher density contrasts between hydrogen and methane at higher depths (Table 8), which increase buoyancy forces.

This is exemplified in Figure S7 for Model 4, where gravity override is more pronounced when the depth is higher.

In general, conducting operations at greater depths can significantly increase storage capacity, but this comes at the cost of slightly lower performance metrics and several operational challenges, such as deep well perforation and the need for larger injected masses. It is important to highlight that these results depend on the operational conditions defined for the high- and low-depth settings; thus, changes in flow rates, initial pressure, pressure constraints, and cycle durations can significantly impact this conclusion.

4.3. Comparison with previous works

Bo et al. (2024) studied the effect of geological factors on gas mixing in a depleted braided-fluvial reservoir. They concluded that geological structure (reservoir dip and closure area) is a first-order factor above facies heterogeneity. Other works (Sainz-Garcia et al., 2017; Okoroafor et al., 2022, e.g.) also recognize the benefit of dipping structures in UHS, as long as the well is placed updip.

Our findings agree that reservoir dip is a first-order factor (Figure 6), but indicate that some stratigraphic heterogeneities, related to thickness and continuity of the layers, are also of first-order relevance. These factors were shown to control the strength of gravity effects and, in the case of the continuity of aeolian bodies, to affect equivalent petrophysical properties.

Okoroafor et al. (2022) analyzed the importance of dip angle, reservoir thickness and depth on the performance of UHS in a homogeneous gas reservoir connected with an aquifer. Besides including heterogeneities and excluding water flow, our approach differs in the performance metrics and the treatment of flow rates. Okoroafor et al. (2022) used the productivity index (PI) as their primary metric, which is the production flow rate per unit pressure drop; moreover, they applied a constant injection rate across all the tested thickness values.

In contrast, we assess performance using RF, MP, FP and total injected and recovered mols of H_2. Furthermore, we scale the injection and production rates according to the reservoir thickness (Section 3.5), ensuring that all the tested models operate at full storage capacity and achieve a comparable proportion of the total pore volume occupied by H_2.

Regarding reservoir depth, our results align with the findings by Okoroafor et al. (2022), who observed a lower PI for higher depths, because of a larger compression energy required to deliver the same flow rate. However, they reached different conclusions concerning reservoir thickness, reporting a decline in performance when the

thickness was either increased or decreased from a reference value. This led to the conclusion that there exists an optimal thickness that maximizes performance.

This discrepancy is likely due to differences in how flow rates were treated. Since Okoroafor et al. (2022) employed a constant target rate across all thicknesses, models with different thicknesses present different fluid velocities and pressure variations. In our analysis, the scaling the flow rates according to thickness ensures that all models operate at comparable ranges of average reservoir pressure (Figure S5) and injected pore volumes. This enables a comparison of performance under similar pressure drops and pore volume injection, isolating the effect of geological factors more effectively.

5. Criteria for screening and ranking

The performance metrics and the flow behavior of the model ensemble indicate that gravity effects are the main mechanism affecting storage performance in the early stages of UHS in depleted gas fields.

The influence of gravity on flow behavior has been extensively considered through various formulations of the gravity number (N_g), which generally quantifies the ratio between buoyancy and viscous forces. The reader is referred to Rahman et al. (2017) for a review of different formulations of the gravity number. The use of this number has been primarily developed in the context of secondary oil recovery, under the assumption of multiphase immiscible flow.

Although the flow and transport of $\mathsf{CH_4}$ and $\mathsf{H_2}$ is not immiscible, our observations reveal a clear interface between hydrogen-rich and methane-rich gas, especially in the early stages of the operation. Moreover, Wang et al. (2022) observed that the gravity number correlates with the recovery of $\mathsf{H_2}$ in numerical simulations performed on heterogeneous samples across different length scales.

We use the following formulation of the gravity number, derived by Shook et al. (1992) for two-dimensional, two-phase flow

$$N_g = \frac{k_x \ \lambda \ \Delta\rho \ g \cos\alpha}{u} \frac{H}{L}, \tag{8}$$

where k_x is the horizontal permeability, λ is the mobility of the injected phase, $\Delta\rho$ is the density difference between the two fluids, g is the gravitational acceleration, α is the dip angle, u is the velocity of the injected fluid, H is the reservoir thickness, and L is the length of the reservoir.

Shook et al. (1992) assumed a homogeneous reservoir. To investigate the correlation of this gravity number with the recovery factors calculated for Cycle 1, we introduce two modifications to account for the heterogeneities in the model ensemble

of the Bunter sandstone. First, since the flow is compartmentalized within similar, repeating depositional cycles, the reservoir thickness H is replaced with the effective flow thickness $H*$, defined as the thickness of a single depositional cycle (Figure 7). Second, the permeability k_x is taken as the upscaled longitudinal permeability computed with flow-based upscaling. Note that in periodic media, the effective permeability of the medium is equal to the permeability computed over a single representative unit cell. Therefore, the permeability computed by RRM for the entire domain should approximate the permeability of a single depositional cycle.

The velocity u_t is computed as the velocity at which the fluid enters the well:

$$u = \frac{q_{rec}}{\rho_{H2}^{BHP_{min}} \pi D_w H}, \tag{9}$$

where q_{rec} is the recovery rate from Table 4, converted to kg/s, $\rho_{H2}^{BHP_{min}}$ is the density of hydrogen at the minimum BHP, $D_w = 0.16$ m is the well diameter, and H is the reservoir thickness. The density difference $\Delta\rho$ is taken as the difference between the densities of hydrogen and methane at the minimum BHP (Table 8). The mobility λ is taken as the inverse of hydrogen viscosity at the same conditions, given that we are dealing with a single-phase flow problem.

Under these assumptions, a strong correlation is observed between the RF of Cycle 1 and N_g, as measured by the Spearman correlation coefficients shown in Figure 13. The Spearman coefficient assesses the monotonic relationship between two variables based on the correlation of their ranked values.

The correlation between RF and N_g is stronger when the data is grouped into high dip and low dip categories. The physical behavior of the models with dip indeed differs from those without dip. While the $cos\alpha$ term in Equation 8 accounts for the buoyancy forces acting in the transversal direction of the reservoir compartments, the high-dip models also benefit from a longitudinal component of the gravitational force. This component, which promotes segregation of methane at the bottom of the reservoir, is not included in N_g.

The gravity number can predict the key results of the numerical simulations, such as the initial loss of performance associated with higher depths and thicker depositional cycles, and the negative impact of higher longitudinal permeabilities on the performance of Cycle 1, which is due to a fast lateral spreading of hydrogen and early production of methane. Mass purity is strongly correlated with the cycle RF, with a Spearman coefficient of 0.96 for Cycle 1; therefore, identifying sites with the highest RF also leads to higher purity. The RF of the first cycle is also strongly correlated with the ultimate RF (Spearman coefficient of 0.97) indicating that early-stage performance is a reliable predictor of the overall performance after several years

of operation.

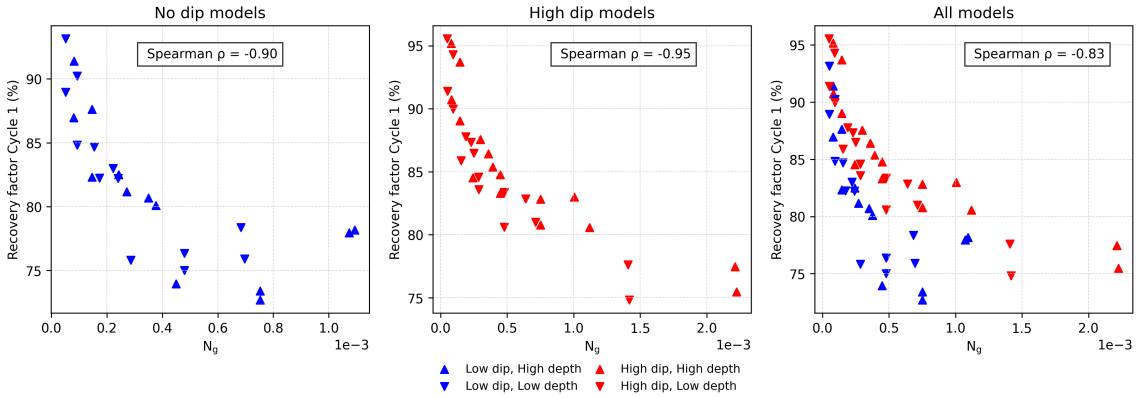

Figure 13: Correlation between the modified gravity number (N_g) and the recovery factor of Cycle 1.

The correlation between the gravity number and the recovery factor in Cycle 1 suggests that the modified N_g could serve as a screening and ranking metric. Its use as a reliable criterion requires further validation through field data and experimental studies. N_g could be integrated into performance screening by following the steps below:

1. Screen for storage capacity: Before assessing recovery performance, it is necessary to ensure that the reservoirs can meet a required storage capacity. The maximum injected mass of hydrogen that can be initially stored depends on the compression of the in-situ gas (CH_4, in this study). Based on the assumption of no-flow boundaries and pressure distributions that are nearly uniform and close to the BHP across the reservoir (Figures S5 and S6), the initial maximum storage capacity of hydrogen can be roughly estimated as:

$$M_{CH4,0} = V\phi_0\rho_{CH4,0}, \tag{10}$$

$$S = \rho_{H2,inj}\left(\frac{V\phi_i}{(1+c_p)\Delta P} - \frac{M_{CH4,0}}{\rho_{CH4,inj}}\right), \tag{11}$$

where $M_{CH4,0}$ is the mass of methane initially in place, V is the reservoir volume, ϕ_i is the initial average porosity, $\rho_{CH4,0}$ and $\rho_{CH4,inj}$ are the methane densities at the initial (depleted) state and at the maximum BHP, respectively, S is the initial storage capacity of hydrogen, c_p is the rock's pore compressibility,

ΔP is the difference between maximum BHP and the initial pressure, and $\rho_{H2,inj}$ is the density of hydrogen at the maximum BHP.

2. Cluster reservoirs according to dip: grouping reservoirs with similar structural dips allows the gravity number to correlate better with performance.

3. Rank reservoir according to the proposed gravity number, giving higher priority to higher dips, provided that the well can be placed up-dip

This procedure has potential as a screening step, not excluding the used of other essential criteria related to socio-economic viability and geological factors not addressed here, such as containment integrity, caprock lithology, and possible hydrogen loss mechanisms.

The proposed screening procedure advances the methodology proposed by Okoroafor et al. (2022) to rate candidate fields, which attributes individual grades to several reservoir features. Our approach improves upon this by accounting for geological heterogeneities and by providing a single integrated criterion - the modified gravity number - that encapsulates the influence of multiple geological factors.

Notably, our results diverge from those of Okoroafor et al. (2022) with respect to the reservoir permeability and thickness. While their procedure favors higher permeability intermediate reservoir thicknesses, the modified gravity number indicates an opposite trend. This change comes with the underlying assumption of the operation at full reservoir capacity, which led to the scaling of flow rates according to the thickness and depth of the reservoir.

6. Conclusions

We evaluated the geological controls on UHS operations using an ensemble of 64 numerical models representing depleted gas reservoirs in the Bunter Sandstone. These models present different geological scenarios by varying factors such as reservoir dip, thickness and depth, and sedimentological heterogeneities.

Using this model ensemble to perform simulations of hydrogen storage operations, we assessed how geology impacts flow behavior and performance metrics related to storage capacity, recovery, and purity. Our main findings are summarized as follows.

- Geological heterogeneities (stratigraphy, reservoir depth, structural dip) contribute most variability to the performance of the UHS operation in its early stages. This variability decreases as the gas (methane) initially in place is recovered and hydrogen has time to invade lower-permeability layers.

- In the first cycles, the performance is governed by the strength of gravity effects, which is controlled by three key geological factors: thickness of facies-association layers, reservoir thickness, and dip angle. Thinner layers weaken buoyancy forces that drive gravity override, while dip angles retard methane production, leaving it segregated at the bottom of the reservoir.

- Small variations in porosity significantly increase the storage capacity. In the low-depth models, an additional 1.2% porosity associated with continuous aeolian bodies results in a 7% increase in storage capacity. Nonetheless, these higher porosities are also linked to greater longitudinal permeabilities, which enhance the lateral spreading of hydrogen and reduce the recovery factor.

- Doubling the depth from 1500 m to 3000 m increases the storage capacity by a factor of 1.6. While greater depth enhances storage potential, it also introduces operational challenges, decreases gas compressibility and increases density contrasts, intensifying gravity effects.

- Mudstone layers in the Bunter Sandstone models compartmentalize the flow vertically, particularly when they exhibit high continuity. As a result, the thickness of a depositional cycle defines the effective vertical distance over which the buoyancy forces act.

- A modified gravity number was proposed to account for the effective thickness for flow, corresponding to the compartments bounded by low permeability layers, and for the effective permeability of the heterogeneous medium. This modified gravity number correlates strongly with performance metrics during the first cycle and could serve as a quick-to-calculate screening criterion, subject to future validation.

Given these findings, a two-stage geological screening approach is suggested. In a primary assessment, candidate reservoirs are screened based on storage capacity, prioritizing lower depths. In a second stage, the candidates are ranked according to the modified gravity number, which accounts for key geological factors. This ranking identifies the reservoirs that are most likely to achieve top performance during the critical early stages of operation, which dictate the overall performance in the long-term.

These conclusions are drawn upon specific operational assumptions: a single fully-perforated vertical well, operation at full storage and recovery capacities under defined pressure constraints, a given initial depletion level, and fixed cycle durations. Future work should assess whether different operational conditions modify the main

geological controls and how they interact with the geological factors investigated in this study.

Acknowledgments

The authors thanks Shell Global Solutions International B.V. for sponsoring this work through ASSET program and granting permission to publish this work. Sebastian Geiger thanks Energi Simulation for supporting his Chair in Sustainable Geoenergy.

References

Agada, S., Chen, F., Geiger, S., Toigulova, G., Agar, S., Shekhar, R., Benson, G., Hehmeyer, O., Amour, F., Mutti, M., Christ, N., Immenhauser, A., 2014. Numerical simulation of fluid-flow processes in a 3d high-resolution carbonate reservoir analogue. Petroleum Geoscience 20, 125–142. doi:10.1144/petgeo2012-096.

Alshakri, J., Hampson, G.J., Jacquemyn, C., Jackson, M.D., Petrovskyy, D., Geiger, S., Silva, J.D., Judice, S., Rahman, F., Sousa, M.C., 2023. A screening assessment of the impact of sedimentological heterogeneity on co2 migration and stratigraphic-baffling potential: Sherwood and bunter sandstones, uk. Geological Society Special Publication 528, 245–266. doi:10.1144/SP528-2022-34.

Amy, L., Peachey, S., Gardiner, A., Pickup, G., Mackay, E., Stephen, K., 2013. Recovery efficiency from a turbidite sheet system: Numerical simulation of waterflooding using outcrop-based geological models. Petroleum Geoscience 19, 123–138. doi:10.1144/petgeo2011-041.

Bentley, M., Smith, S., 2008. Scenario-based reservoir modelling: The need for more determinism and less anchoring. Geological Society, London, Special Publications 309, 145–159. doi:10.1144/SP309.11.

Bo, Z., Hörning, S., Underschultz, J.R., Garnett, A., Hurter, S., 2024. Effects of geological heterogeneity on gas mixing during underground hydrogen storage (UHS) in braided-fluvial reservoirs. Fuel 357. doi:10.1016/j.fuel.2023.129949.

Cleijne, H., de Ronde, M., Duvoort, M., de Kleuver, W., Raadschelders, J., 2020. North sea energy outlook.

Daniilidis, A., Saeid, S., Doonechaly, N.G., 2021. The fault plane as the main fluid pathway: Geothermal field development options under subsurface and operational uncertainty. Renewable Energy 171, 927–946. URL: https://www.sciencedirect.com/science/article/pii/S096014812100327X, doi:https://doi.org/10.1016/j.renene.2021.02.148.

Department of Energy and Climate Change, 2011. UK renewable energy roadmap.

Delft High Performance Computing Centre (DHPC), 2024. DelftBlue Supercomputer (Phase 2). https://www.tudelft.nl/dhpc/ark:/44463/DelftBluePhase2.

Diamantakis, N., Peecock, A., Shahrokhi, O., Pitchaimuthu, S., Andresen, J.M., 2024. A review of analogue case studies relevant to large-scale underground hydrogen storage. Energy Reports 11, 2374–2400. doi:10.1016/j.egyr.2024.02.002.

van Eijk, M.M., 2014. Volpriehausen prospectivity review. MSc thesis, VU University Amsterdam .

Flemisch, B., Nordbotten, J.M., Fernø, M., et al., 2024. The fluidflower validation benchmark study for the storage of co_2. Transport in Porous Media 151, 865–912. doi:10.1007/s11242-023-01977-7.

Geluk, M., Röhling, H.G., 1997. High-resolution sequence stratigraphy of the Lower Triassic Buntsandstein in the Netherlands and Northwestern Germany. Geologie en Mijnbouw 76, 227–246. doi:10.1023/A:1003062521373.

Graham, G.H., Jackson, M.D., Hampson, G.J., 2015. Three-dimensional modeling of clinoforms in shallow-marine reservoirs: Part 1. concepts and application. AAPG Bulletin 99, 1013–1047. doi:10.1306/01191513190.

Harati, S., Rezaei Gomari, S., Ramegowda, M., Pak, T., 2024. Multi-criteria site selection workflow for geological storage of hydrogen in depleted gas fields: A case for the uk. International Journal of Hydrogen Energy 51, 143–157. doi:https://doi.org/10.1016/j.ijhydene.2023.10.345.

Hassanpouryouzband, A., Joonaki, E., Edlmann, K., Heinemann, N., Yang, J., 2020. Thermodynamic and transport properties of hydrogen containing streams. Scientific Data 7, 222. URL: https://doi.org/10.1038/s41597-020-0568-6, doi:10.1038/s41597-020-0568-6.

de Hoop, S., Voskov, D., Ahusborde, E., et al., 2024. A benchmark study on reactive two-phase flow in porous media: Part i - model description. Computational Geosciences 28, 175–189. doi:10.1007/s10596-024-10268-z.

Huber, M., 2018. Models for viscosity, thermal conductivity, and surface tension of selected pure fluids as implemented in refprop v10.0. doi:https://doi.org/10.6028/NIST.IR.8209.

Jackson, M.D., Hampson, G.J., Sech, R.P., 2009. Three-dimensional modeling of a shoreface-shelf parasequence reservoir analog: Part 2. geologic controls on fluid flow and hydrocarbon recovery. AAPG Bulletin 93, 1183–1208. URL: https://doi.org/10.1306/05110908145, doi:10.1306/05110908145.

Jackson, W.A., Hampson, G.J., Jacquemyn, C., Jackson, M.D., Petrovskyy, D., Geiger, S., Machado Silva, J.D., Judice, S., Rahman, F., Costa Sousa, M., 2022. A screening assessment of the impact of sedimentological heterogeneity on co2 migration and stratigraphic-baffling potential: Johansen and cook formations, northern lights project, offshore norway. International Journal of Greenhouse Gas Control 120, 103762. URL: https://www.sciencedirect.com/science/article/pii/S1750583622001803, doi:https://doi.org/10.1016/j.ijggc.2022.103762.

Jacquemyn, C., Pataki, M.E.H., Hampson, G.J., Jackson, M.D., Petrovskyy, D., Geiger, S., Marques, C.C., Machado Silva, J.D., Judice, S., Rahman, F., Costa Sousa, M., 2021. Sketch-based interface and modelling of stratigraphy and structure in three dimensions. Journal of the Geological Society 178, jgs2020–187. doi:10.1144/jgs2020-187.

Juez-Larré, J., van Gessel, S., Dalman, R., Remmelts, G., Groenenberg, R., 2019. Assessment of underground energy storage potential to support the energy transition in the netherlands. First Break 37, 57–66. doi:https://doi.org/10.3997/1365-2397.n0039.

van Kempen, B.M.M., Mijnlieff, H.F., van der Molen, J., 2018. Data mining in the dutch oil and gas portal: a case study on the reservoir properties of the volpriehausen sandstone interval. Geological Society, London, Special Publications 469, 253–267. doi:10.1144/SP469.1.

Kobeissi, S., Ling, N.N., Yang, K., May, E.F., Johns, M.L., 2024. Dispersion of hydrogen in different potential cushion gases. International Journal of Hydrogen Energy 60, 940–948. doi:10.1016/j.ijhydene.2024.02.151.

Korevaar, S., Dalman, R., Nelskamp, S., Atkins, S., Boter, E., Wiarda, E., Nolten, M., Beintema, K., 2023. Play 5 triassic. https://www.geodeatlas.nl/pages/play-5-triassic. Accessed: 04 07, 2025.

Lankof, L., Luboń, K., Gallo, Y.L., Tarkowski, R., 2024. The ranking of geological structures in deep aquifers of the polish lowlands for underground hydrogen storage. International Journal of Hydrogen Energy 62, 1089–1102. doi:10.1016/j.ijhydene.2024.03.106.

Lemmon, E.W., Bell, I.H., Huber, M.L., McLinden, M.O., 2025. Thermophysical properties of fluid systems. NIST Chemistry WebBook, NIST Standard Reference Database Number 69. doi:10.18434/T4D303. retrieved April 10, 2025.

Lyu, X., Khait, M., Voskov, D., 2021. Operator-based linearization approach for modeling of multiphase flow with buoyancy and capillarity. SPE Journal 26, 1858 – 1878. doi:10.2118/205378-PA.

Medici, G., West, L., Mountney, N., 2018. Sedimentary flow heterogeneities in the Triassic U.K. Sherwood sandstone group: Insights for hydrocarbon exploration. Geological Journal 54. doi:10.1002/gj.3233.

Navaid, H.B., Emadi, H., Watson, M., 2023. A comprehensive literature review on the challenges associated with underground hydrogen storage. International Journal of Hydrogen Energy 48, 10603–10635. URL: https://www.sciencedirect.com/science/article/pii/S0360319922055446, doi:https://doi.org/10.1016/j.ijhydene.2022.11.225.

Netherlands Oil and Gas Portal (NLOG), . Temperature data. https://www.nlog.nl/en/temperature-data. Accessed: 2025-04-08.

Newell, A., 2017. Evolving stratigraphy of a middle triassic fluvial-dominated sheet sandstone: The otter sandstone formation of the wessex basin (uk). Geological Journal 53, 1654–1971. doi:10.1002/gj.3026.

Nordbotten, J.M., Fernø, M.A., Flemisch, B., Kovscek, A.R., Lie, K.A., Both, J.W., Møyner, O., Sandve, T.H., Ahusborde, E., Bauer, S., Chen, Z., Class, H., Di, C., Ding, D., Element, D., Flauraud, E., Franc, J., Gasanzade, F., Ghomian, Y., Giddins, M.A., Green, C., Fernandes, B.R., Hadjisotiriou, G., Hammond, G., Huang, H., Kachuma, D., Kern, M., Koch, T., Krishnamurthy, P., Lye, K.O., Landa-Marbán, D., Nole, M., Orsini, P., Ruby, N., Salinas, P., Sayyafzadeh, M., Torben, J., Turner, A., Voskov, D.V., Wendel, K., Youssef, A.A., 2025. Benchmarking co storage simulations: Results from the 11th society of petroleum engineers

comparative solution project. International Journal of Greenhouse Gas Control 148, 104519. URL: https://www.sciencedirect.com/science/article/pii/S1750583625002178, doi:https://doi.org/10.1016/j.ijggc.2025.104519.

Okoroafor, E.R., Saltzer, S.D., Kovscek, A.R., 2022. Toward underground hydrogen storage in porous media: Reservoir engineering insights. International Journal of Hydrogen Energy 47, 33781–33802. doi:10.1016/j.ijhydene.2022.07.239.

Petrovskyy, D., Jacquemyn, C., Geiger, S., Jackson, M.D., Hampson, G.J., Silva, J.D.M., Judice, S., Rahman, F., Sousa, M.C., 2023. Rapid flow diagnostics for prototyping of reservoir concepts and models for subsurface co2 storage. International Journal of Greenhouse Gas Control 124. doi:10.1016/j.ijggc.2023.103855.

Pfeiffer, W.T., Beyer, C., Bauer, S., 2017. Hydrogen storage in a heterogeneous sandstone formation: Dimensioning and induced hydraulic effects. Petroleum Geoscience 23, 315–326. doi:10.1144/petgeo2016-050.

Rahman, A., Happy, F.A., Ahmed, S., Hossain, M.E., 2017. Development of scaling criteria for enhanced oil recovery: A review. Journal of Petroleum Science and Engineering 158, 66–79. doi:https://doi.org/10.1016/j.petrol.2017.08.040.

Ringrose, P., Bentley, M., 2015. Reservoir Model Design: A Practitioner's Guide. 1 ed.. Springer Dordrecht. p. 26. doi:10.1007/978-94-007-5497-3.

Safari, A., Sugai, Y., Sarmadivaleh, M., Imai, M., 2023. Screening and ranking japanese gas fields for underground h2 storage potential: Impact of the reservoir drive mechanism. Journal of Energy Storage 70, 107679. doi:https://doi.org/10.1016/j.est.2023.107679.

Sainz-Garcia, A., Abarca, E., Rubi, V., Grandia, F., 2017. Assessment of feasible strategies for seasonal underground hydrogen storage in a saline aquifer. International Journal of Hydrogen Energy 42, 16657–16666. doi:10.1016/j.ijhydene.2017.05.076.

Shook, M., Li, D., Lake, L., 1992. Scaling immiscible flow through permeable media by inspectional analysis. In Situ-NY 16:4, 311–349.

Tarkowski, R., 2019. Underground hydrogen storage: Characteristics and prospects. Renewable and Sustainable Energy Reviews 105, 86–94. doi:10.1016/j.rser.2019.01.051.

Voskov, D., Saifullin, I., Novikov, A., Wapperom, M., Orozco, L., Seabra, G.S., Chen, Y., Khait, M., Lyu, X., Tian, X., De Hoop, S., Palha, A., 2024. open delft advanced research terra simulator(open-DARTS) 9, 6737. URL: https://joss.theoj.org/papers/10.21105/joss.06737, doi:10.21105/joss.06737.

Wang, G., Pickup, G., Sorbie, K., Mackay, E., 2022. Scaling analysis of hydrogen flow with carbon dioxide cushion gas in subsurface heterogeneous porous media. International Journal of Hydrogen Energy 47, 1752–1764. doi:10.1016/j.ijhydene.2021.10.224.

Wang, Y., Voskov, D., Khait, M., Bruhn, D., 2020. An efficient numerical simulator for geothermal simulation: A benchmark study. Applied Energy 264, 114693. URL: https://www.sciencedirect.com/science/article/pii/S0306261920302051, doi:https://doi.org/10.1016/j.apenergy.2020.114693.

Xinyu, D., J., H., Jacquemyn, C., Jackson, M., Petrovskyy, D., Geiger, S., Wang, Y., 2025. Screening assessment of the impact of structural and sedimentary geological heterogeneities on the performance of an ultra-deep carbonate reservoir, north-central tarim basin, northwest china. Journal of Geoenergy 2025, Art no. 4610521. doi:10.1155/jge5/4610521.

Zivar, D., Kumar, S., Foroozesh, J., 2021. Underground hydrogen storage: A comprehensive review. International Journal of Hydrogen Energy 46, 23436–23462. URL: https://www.sciencedirect.com/science/article/pii/S0360319920331426, doi:https://doi.org/10.1016/j.ijhydene.2020.08.138. hydrogen Separation, Production and Storage.

Supplementary Material - Geological controls on Underground Hydrogen Storage in depleted gas fields

1. Estimation of low and high settings in the Design of Experiment

In our extended DOE, the low and high settings for reservoir dip, depth, and thickness were derived from the well log and core sample dataset compiled by Korevaar et al. (2023), made available through a Triassic play map and accompanying ArcGIS files.

Our estimates are based on the visual analysis of the Triassic Play Map and on borehole data in ArcGIS for wells intersecting gas fields, as exemplified in Figure S1.

The low and high values for reservoir thickness were estimated based on the *Net thickness of stacked Triassic reservoirs* indicated in the Triassic play map. Most Triassic gas fields lie within the contours for the ranges of 50-75m and 150-200m. Accordingly, we retained 176m—corresponding to the original geological models—as the high thickness setting and defined the low thickness setting as one-third of this value, i.e., 59m.

Depth settings were based on the *Top Depth* data from filtered wells in the ArcGIS dataset. A total of 56 gas fields were included in this analysis. The 10% and 90% percentiles of these depth values were 1460m and 3350m, respectively. Based on these results, the low and high depth settings are defined as equal to 1500m and 3000m, respectively.

Dip settings were estimated for individual fields that had at least three spatially distributed wells with available *Top Depth* data. For these fields, we interpolated a plane through the coordinates of the top depths (Figure S1). Fields with an interpolation R^2 coefficient greater than 0.6 were retained, and dip was estimated as the minimum inclination angle of the interpolated plane. A total of 15 fields met this criterion. The 10% and 90% percentiles of the resulting dip angles were 0.3° and 3.2°, respectively. These values guided the selection of dip settings in our models, defined as 0° (low) and 3° (high).

2. Supplementary Figures

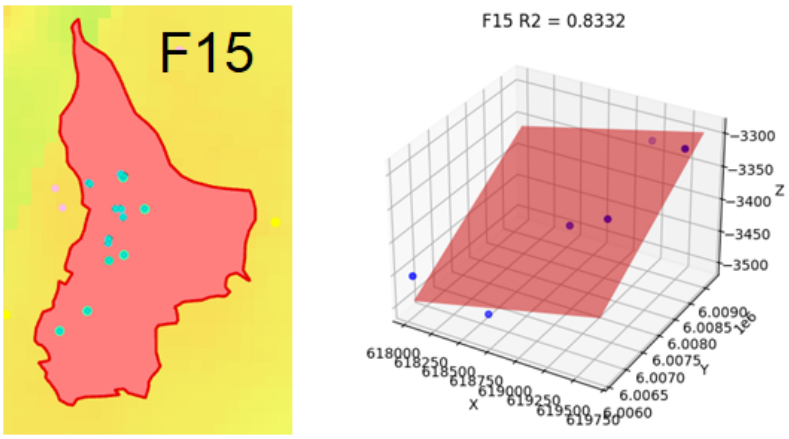

Figure S1: Example of filtering of the wells that pass through field F15 (left) and the use of the ones with data for *Top Depth* to interpolate a plan for the estimation of dips (right).

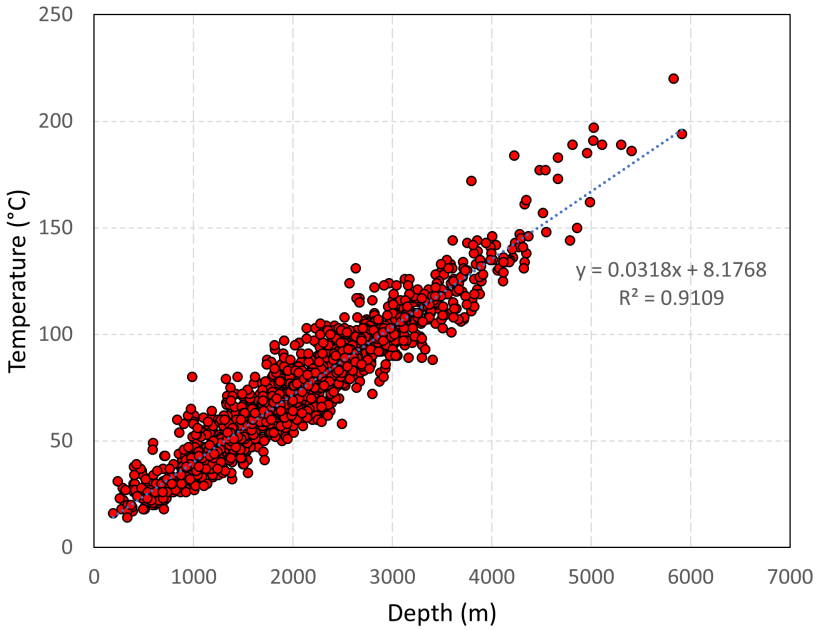

Figure S2: Bore hole temperature vs. depth as obtained from the Netherlands Oil and Gas Portal, and linear interpolation performed to estimate the temperatures in the numerical models.

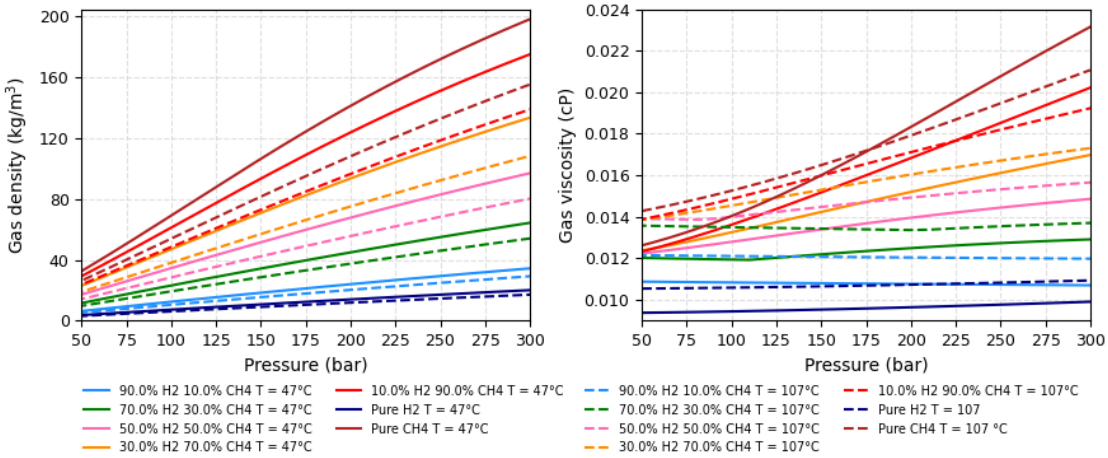

Figure S3: Fluid properties used in open-DARTS for the gaseous mixture of H_2 and CH_4: the density computed with a Peng-Robinson model (left), and the dataset for viscosity as computed by Hassanpouryouzband et al. (2020) using the SuperTRAPP model (right). The properties are calculated for the pressure-temperature range used in the simulations.

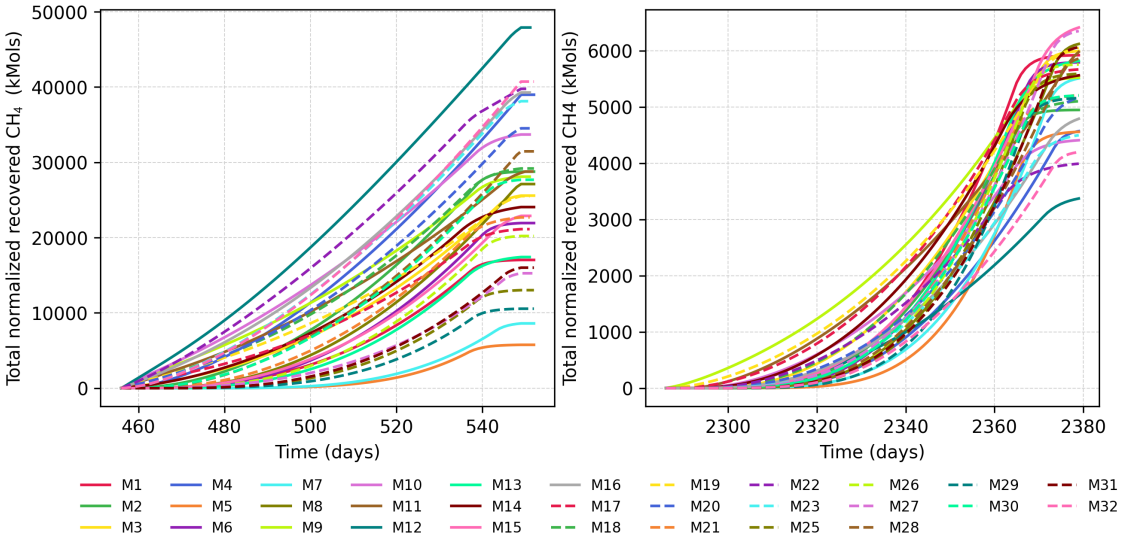

Figure S4: Production of methane for the model ensemble in the first (left) and last (right) simulated withdrawal periods.

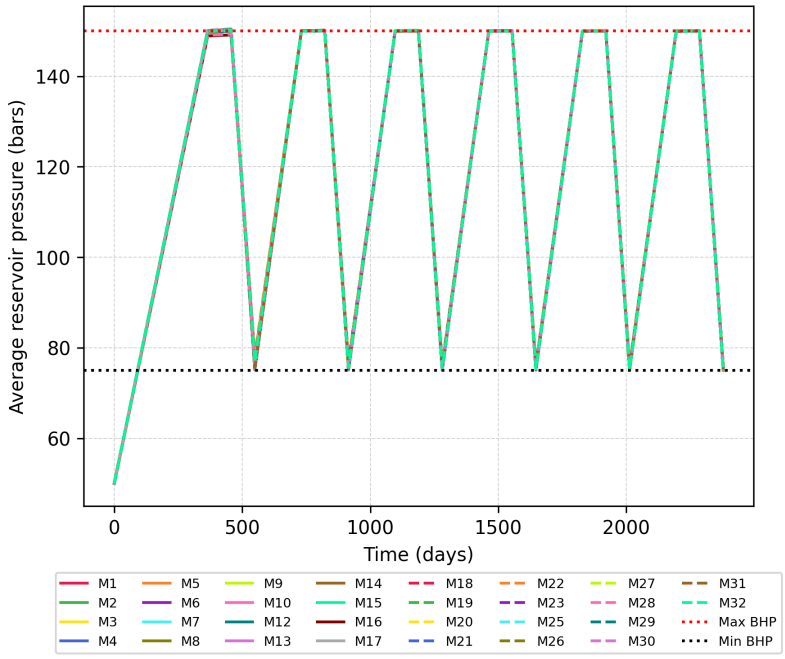

Figure S5: Average reservoir pressure computed for the ensemble of low-depth models. The average reservoir pressure varies between the minimum and maximum BHPs, which correspond to 75 bar and 150 bar, respectively, and are indicated in the dotted lines.

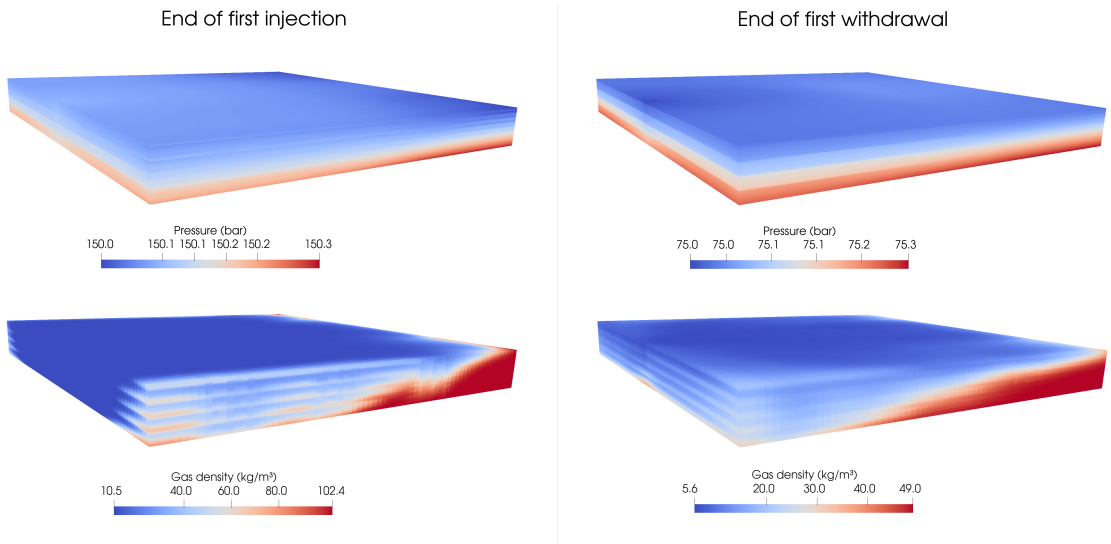

Figure S6: Gas pressure and densities for Model 1 at the end of the first injection and withdrawal. The reservoir pressure is always nearly constant and close fo the BHP.

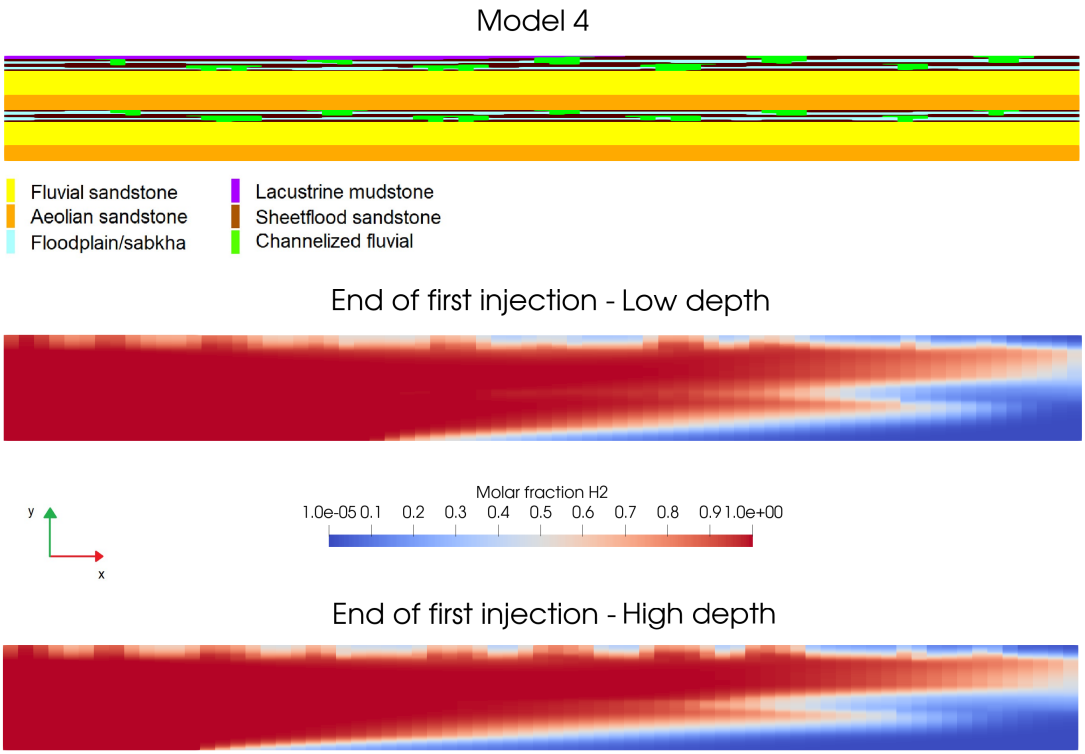

Figure S7: Cross section of the geological model of Model 4 and of the distribution of the H_2 plume at the end of the first injection for the low and high depth cases. In the high depth scenario, gravity override is more pronounced, as evidenced by the higher lateral extent of the methane plume at the bottom of the reservoir.